Metamorphic CO2 Production in Collisional Orogens: Petrological Constraints from Phase Diagram Modeling of Himalayan, Scapolite-bearing, Calc-silicate Rocks in the NKC(F)MAS(T)-HC system

(Article begins on next page)

17 April 2024

Author Query Form

AUTHOR QUERIES – TO BE ANSWERED BY THE CORRESPONDING AUTHOR

The following queries have arisen during the typesetting of your manuscript. Please click on each query number and respond by indicating the change required within the text of the article. If no change is needed please add a note saying "No change."

AQ1:   Groppo et al. 2013 - should this be 2013a or 2013b, or both?

AQ2:   Kellet et al. 2010 - spelling of author's name is not as in reference list. Which is the correct version?

AQ3:   'revised 2008' - please cite the reference for this, and add publication details to reference list

AQ4:   Please confirm change to 'and is replaced by' is OK

AQ5:   Burchfield et al. 1992 - please add editor/s and title of Special Paper

AQ6:   Pouchou & Pichoir 1988 - please add book editor/s

AQ7:   Rolfo et al. 2015 - please add the other editors' names

AQ8:   Rolfo et al. 2017 - please update this reference if possible

AQ9:   Fig. 7 - the dotted lines do not show up clearly in figure; please amend the symbol

AQ10: Please check that all names have been spelled correctly and appear in the correct order. Please also check that all initials are present. Please check that the author surnames (family name) have been correctly identified by a pink background. If this is incorrect, please identify the full surname of the relevant authors. Occasionally, the distinction between surnames and forenames can be ambiguous, and this is to ensure that the authors' full surnames and forenames are tagged correctly, for accurate indexing online. Please also check all author affiliations.

MAKING CORRECTIONS TO YOUR PROOF

These instructions show you how to mark changes or add notes to your proofs using Adobe Acrobat Professional versions 7 and onwards, or Adobe Reader DC. To check what version you are using go to **Help** then **About**. The latest version of Adobe Reader is available for free from get.adobe.com/reader.
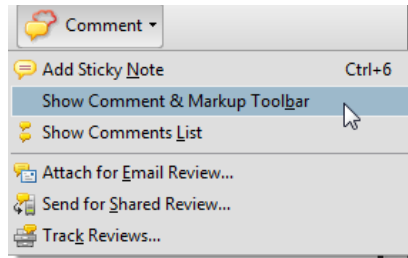
DISPLAYING THE TOOLBARS

Adobe Reader DC
In Adobe Reader DC, the Comment toolbar can be found by clicking 'Comment' in the menu on the right-hand side of the page (shown below).

The toolbar shown below will then display along the top.
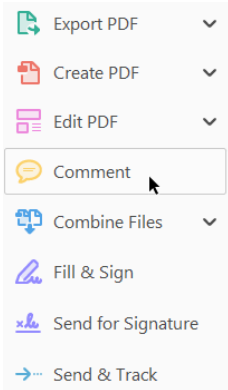
Acrobat Professional 7, 8, and 9
In Adobe Professional, the Comment toolbar can be found by clicking 'Comment(s)' in the top toolbar, and then clicking 'Show Comment & Markup Toolbar' (shown below).

The toolbar shown below will then be displayed along the top.

USING TEXT EDITS AND COMMENTS IN ACROBAT
This is the quickest, simplest and easiest method both to make corrections, and for your corrections to be transferred and checked.
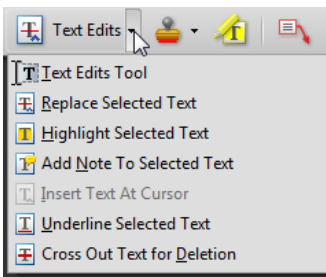
1. Click **Text Edits**
2. Select the text to be annotated or place your cursor at the insertion point and start typing.
3. Click the **Text Edits** drop down arrow and select the required action.

You can also right click on selected text for a range of commenting options, or add sticky notes.

SAVING COMMENTS
In order to save your comments and notes, you need to save the file (**File, Save**) when you close the document.

USING COMMENTING TOOLS IN ADOBE READER
All commenting tools are displayed in the toolbar. You cannot use text edits, however you can still use highlighter, sticky notes, and a variety of insert/replace text options.

POP-UP NOTES
In both Reader and Acrobat, when you insert or edit text a pop-up box will appear. In **Acrobat** it looks like this:
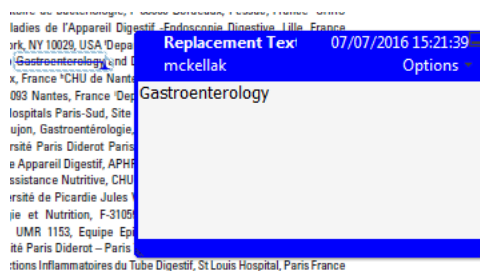
In **Reader** it looks like this, and will appear in the right-hand pane:
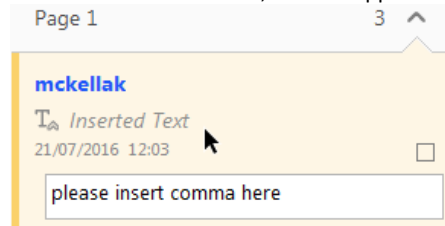
DO NOT MAKE ANY EDITS DIRECTLY INTO THE TEXT, USE COMMENTING TOOLS ONLY.

Metamorphic CO$_2$ Production in Collisional Orogens: Petrological Constraints from Phase Diagram Modeling of Himalayan, Scapolite-bearing, Calc-silicate Rocks in the NKC(F)MAS(T)-HC system

AQ10

Chiara Groppo[1,2]*, Franco Rolfo[1,2], Daniele Castelli[1] and Pietro Mosca[2]

[1]Department of Earth Sciences, University of Torino, Via Valperga Caluso 35, 10125 Turin, Italy; [2]IGG-CNR, Via Valperga Caluso 35, 10125 Turin, Italy

*Corresponding author. Telephone: +39 0116705106. Fax: +39 0116705128. E-mail: chiarra.groppo@unito.it

ABSTRACT

A reliable quantitative estimate of the metamorphic CO$_2$ flux from collisional orogens is fundamental to our understanding of the deep carbon cycle, but it is still far from being constrained. Among major uncertainties are the poor knowledge of the nature of metamorphic CO$_2$-producing processes and the amount of CO$_2$ potentially released through these reactions. Previous studies of metamorphic decarbonation reactions in metacarbonate rocks mainly used simple model reactions between end-members in simplified model systems. However, fully quantitative modelling of calc-silicate rocks requires an investigation of very complex systems with more than six components. Moreover, scapolite solid solution has been rarely included in previous studies, although this mineral is often a major constituent of calc-silicate rocks. This study focuses on (1) the CO$_2$-producing processes occurring in scapolite-bearing calc-silicate rocks and (2) the discussion of a methodological approach suitable to understand and quantify these processes. In this framework, phase relations and devolatilization reactions in the Na$_2$O–K$_2$O–CaO–(FeO)–MgO–Al$_2$O$_3$–SiO$_2$–(TiO$_2$)–H$_2$O–CO$_2$ [NKC(F)MAS(T)-HC] system are considered, with application to high-grade clinopyroxene + calcite + K-feldspar + scapolite + plagioclase + zoisite calc-silicate rocks from the Himalaya. The NKC(F)MAS(T)-HC equilibria involving scapolite and plagioclase solid solutions are investigated using (1) isobaric T–X(CO$_2$) phase diagram sections and pseudosections and (2) mixed-volatile P–T phase diagram projections. This phase diagram approach allowed us to identify scapolite-bearing, CO$_2$-producing, univariant (i.e. isobaric invariant) equilibria that have never been recognized before, and that could not be detected without considering Na–Ca solid solutions in the calculations. It is demonstrated that the investigated calc-silicate rocks behaved as a nearly closed, internally buffered, system during prograde metamorphism and that most of the observed key microstructures correspond to isobaric univariant or invariant assemblages. In such a nearly closed system, the fluid was mostly produced during prograde heating at the isobaric invariant points, where abrupt changes in mineral modes also occurred. The proposed phase diagram approach further allows quantitative estimation of the amount and composition of the fluid produced at such isobaric invariant points. On average, 2·5 mol of CO$_2$ (110 g) per 1000 cm^3 of reacting rock were produced during prograde metamorphism of this calc-silicate rock-type. Because similar scapolite-bearing calc-silicate rocks are abundant in the Himalayan orogen, it is suggested that this calc-silicate rock-type might have produced large amounts of CO$_2$-rich fluids during Himalayan metamorphism. A preliminary estimate of these amounts at the scale of the whole orogen suggests a total metamorphic CO$_2$ production of $\sim(2–7) \times 10^{17}$ mol, corresponding to $(1–3) \times 10^{10}$ Mt of CO$_2$. Integrated over $\sim$20 Myr (i.e. the maximum duration of prograde metamorphism), the

calculated metamorphic CO_2 flux would be $(1\cdot1–3\cdot4) \times 10^{10}$ mol a^{-1}, corresponding to an annual mass flux of $(0\cdot5–1\cdot5) \times 10^3$ Mt a^{-1}. Nevertheless, further studies are still needed to assess more precisely the amount of CO_2 released during the Himalayan orogeny.

Key words: calc-silicate rocks; Himalaya; metamorphic CO_2 production; orogenic CO_2 cycle; phase petrology

INTRODUCTION

Recent studies suggest that metamorphic degassing from active collisional orogens supplies a significant amount of CO_2 to the atmosphere, thus playing a fundamental role in the Earth's carbon cycle (e.g. Becker et al., 2008; Gaillardet & Galy, 2008; Perrier et al., 2009; Evans, 2011; Skelton, 2011; Girault et al., 2014). Quantifying the past-to-present metamorphic CO_2 flux from orogenic zones is therefore fundamental for our understanding of the deep carbon cycle (e.g. Mörner & Etiope, 2002) and of the possible influence exerted by mountain-building processes on the past, present and future climate.

In addition to the possibility of CO_2 degassing through contact metamorphism of impure limestone and shales associated with the emplacement of large igneous provinces (e.g. Ganino & Arndt, 2009; Svensen & Jamtveit, 2010; Ganino et al., 2014), larger amounts of CO_2 may be produced during regional metamorphism in collisional contexts, where decarbonation reactions occur at relatively high temperatures within carbonate-bearing metasediments (e.g. calc-silicate rocks, impure marbles). In these rocks, often representing the metamorphic product of marly intercalations within pelitic sedimentary sequences, CO_2 production is mainly triggered by prograde metamorphic reactions involving carbonates and silicates.

A reliable quantitative estimate of the metamorphic CO_2 flux from collisional orogens is still far from being constrained (e.g. Mörner & Etiope, 2002; Evans, 2011, and references therein). As well as the limited and incomplete information on the relative volumes of potential CO_2-source rocks in collisional orogens (e.g. Rolfo et al., 2017), one of the major uncertainties of the orogenic deep carbon cycle is the still poor knowledge of the nature of metamorphic CO_2-producing processes, and of the amount of metamorphic CO_2 potentially released through these reactions. Previous studies aimed at constraining the metamorphic CO_2 flux related to regional metamorphism (e.g. Kerrick & Caldeira, 1993) mainly used simple model reactions between end-members in the $CaO–Al_2O_3–SiO_2–H_2O–CO_2$ (CAS-HC) or $CaO–MgO–Al_2O_3–SiO_2–H_2O–CO_2$ (CMAS-HC) system (e.g. $Dol + Qz + H_2O \rightarrow Tr + Cal + CO_2$; $Dol + Qz \rightarrow Di + CO_2$; $An + Cal + Qz \rightarrow Grs + CO_2$). However, natural calc-silicate rocks are much more complex than the CAS-HC and CMAS-HC model systems, because of the common occurrence of Ca–Mg–Fe solid solutions (e.g. garnet, clinopyroxene, amphibole), as well as of K

silicates (e.g. biotite, muscovite, K-feldspar) and Ca–Na silicates (e.g. plagioclase, scapolite). A fully quantitative modelling of calc-silicate rocks thus requires investigation of the highly complex nine-component $Na_2O–K_2O–CaO–FeO–MgO–Al_2O_3–SiO_2–H_2O–CO_2$ (NKCFMAS-HC) system (e.g. Bucher & Grapes, 2011): a comprehensive approach to calc-silicate petrogenesis is therefore a formidable task (Winter, 2010).

Different approaches have been traditionally used to address the issue of metamorphic CO_2 production related to regional or local (i.e. contact) metamorphism. A first approach is based on the measured progress of devolatilization reactions and allows the calculation of a volumetric, time-integrated flux. This approach was first developed by Ferry (1980) and successfully applied by Ferry and co-workers and by other researchers in the following decades (e.g. Ferry, 1986, 1992, 1994; Ague & Rye, 1999; Ague, 2000, 2003; Ferry et al., 2013). The 'reaction progress' approach requires estimating the extent ('progress') of metamorphic reactions (generally by analysing the mineralogical changes between the studied samples and their protoliths) and modelling mineral–fluid reactions. This method is particularly suitable to investigate the metamorphic CO_2 flux in contact aureoles and/or regional Barrovian- or Buchan-type terranes, where a progressively higher metamorphic grade affected crustal sequences whose protoliths are relatively well known and do not differ significantly as a function of depth. This method has been generally applied to relatively open systems, where decarbonation reactions were driven by reactive fluid infiltration.

A second approach, less frequently used, is based on phase diagram modelling [mainly $T–X(CO_2)$ grids, more rarely mixed-volatile $P–T$ diagrams] combined with estimates of the mineral modes in the investigated samples. The 'phase diagram' approach is particularly suitable for monitoring changes in fluid composition with changing P and T (e.g. during the prograde evolution). It allows us to constrain the $P–T–X(CO_2)$ evolution of the studied rocks (i.e. to determine the sequence of devolatilization reactions that have occurred as a function of P and T) and to eventually estimate the volume and composition of the fluid released during this evolution. This approach is most useful for the study of regional metamorphism and for systems in which fluid composition is not externally controlled (i.e. internally buffered systems) (e.g. Connolly & Trommsdorff, 1991; Connolly et al., 1994; Groppo et al., 2013), although it was also successfully applied on systems characterized

AQ1

by a significant fluid infiltration (e.g. Schmädicke *et al.*, 2001). The present study uses the latter approach (i.e. 'phase diagram' method).

We focus on (1) the CO_2-producing processes occurring in complex, scapolite-bearing, calc-silicate rocks and (2) the discussion of a methodological approach suitable to understand and quantify these processes. We investigate phase relations and devolatilization reactions in the 10-component Na_2O–K_2O–CaO–(FeO)–MgO–Al_2O_3–SiO_2–(TiO_2)–H_2O–CO_2 NKC(F)MAS(T)-HC system, with application to the high-grade, clinopyroxene + calcite + K-feldspar + scapolite + plagioclase + zoisite calc-silicate rocks from the Greater Himalayan Sequence of eastern Nepal Himalaya. The NKC(F)MAS(T)-HC equilibria involving plagioclase and scapolite Na–Ca solid solutions, zoisite, clinopyroxene, amphibole, chlorite, K-feldspar, muscovite, biotite, quartz, calcite (+ dolomite, paragonite, garnet and wollastonite) and a simple binary H_2O–CO_2 fluid are investigated using (1) isobaric *T*–*X*(CO_2) phase diagram sections and pseudosections and (2) mixed-volatile *P*–*T* phase diagram projections. The fluid behaviour (i.e. buffering in a closed system vs buffering accompanied by infiltration) is discussed by comparing the results of thermodynamic modelling with the observed modes and microstructures. Finally, the amounts and compositions of the fluids produced by the relevant reactions are constrained, and a first-order extrapolation of these amounts to the scale of the whole Himalayan belt is provided.

GEOLOGICAL SETTING

In the eastern Nepal Himalaya, calc-silicate rocks are widespread in the lower and upper structural levels of the Greater Himalayan Sequence (GHS) (e.g. Goscombe *et al.*, 2006; Mosca *et al.*, 2012, 2014; Groppo *et al.*, 2013*b*; Rolfo *et al.*, 2015, 2017). The Greater Himalayan Sequence, bounded to the north by the South Tibetan Detachment System (Burchfield *et al.*, 1992; Carosi *et al.*, 1998; Kellet *et al.*, 2010), consists from lower to upper structural levels of the following: (1) medium- to high-grade metasediments and granitic orthogneisses, whose metamorphic grade increases structurally upward from the staurolite zone to the sillimanite zone and, locally, to anatexis (i.e. the so-called Main Central Thrust Zone; e.g. Goscombe *et al.*, 2006; Searle *et al.*, 2008; Groppo *et al.*, 2009, 2010; Mosca *et al.*, 2012, 2014; Lower Greater Himalayan Sequence in Fig. 1a); (2) high-grade para- and orthogneisses (also called Higher Himalayan Crystallines; e.g. Lombardo *et al.*, 1993; Pognante & Benna, 1993; Upper Greater Himalayan Sequence in Fig. 1a), often anatectic, hosting networks and lens-shaped bodies of leucogranite (e.g. Visonà & Lombardo, 2002). These high-grade gneisses are characterized by a progressive decrease in peak pressure structurally upward, marked by the progressive disappearance of garnet and kyanite and by the appearance of cordierite (e.g. Lombardo *et al.*, 1993; Pognante & Benna, 1993; Groppo *et al.*, 2012, 2013*a*).

In the structurally upper portion of the GHS, calc-silicate rocks, derived from former marly intercalations within a thick sedimentary sequence, are hosted in anatectic, biotite + alkali feldspar + plagioclase + garnet + sillimanite ± kyanite paragneisses (regionally known in eastern Nepal as Barun Gneiss and Jannu–Kangchenjunga Gneiss; e.g. Bordet, 1961; Lombardo *et al.*, 1993; Goscombe *et al.*, 2006). The *P*–*T* evolution of the anatectic paragneiss hosting the calc-silicate rocks studied here has been tightly constrained by Groppo *et al.* (2012) (i.e. their sample 07–35); it is characterized by an almost isobaric prograde heating at *c.* 9 kbar, from ∼550°C to peak conditions of 780–800°C, followed by nearly isothermal decompression to about 6·5 kbar, and then by final cooling and exhumation.

The studied sample 07–22 was collected near Langmale Kharka [27°47′52·0″N, 87°07′33·3″E, 4470 m above sea level (a.s.l.)] in the Barun Valley along the path leading to the Makalu base camp (Fig. 1a). This sample is representative of the most abundant calc-silicate type at this structural level of the GHS (Rolfo *et al.*, 2017). Here, calc-silicate rocks crop out as hundreds of metres thick, intensely folded and/or boudinaged layers (Fig. 1b) hosted within anatectic paragneiss, and are locally cross-cut by discordant decimetre-thick leucogranite dykes (Fig. 1c). At the outcrop scale, these rocks show a different style of folding compared with the host quartzo-feldspathic rocks, because of the strong rheology contrast. The studied sample is characterized by a banded structure, defined by whitish, carbonate-rich centimetric horizons alternating with greenish, clinopyroxene-rich layers of similar thickness (Fig. 1c).

METHODS

Micro-X-ray fluorescence (μ-XRF) maps

The micro-XRF map of an entire thin section (Fig. 2a–d) was acquired using a μ-XRF Eagle III-XPL spectrometer equipped with an energy-dispersive spectroscopy (EDS) Si(Li) detector and an Edax Vision32 microanalytical system (Department of Earth Sciences, University of Torino, Italy). The operating conditions were as follows: 100 ms counting time, 40 kV accelerating voltage and a probe current of 900 μA. A spatial resolution of about 65 μm in both *x* and *y* directions was used. Quantitative modal percentages of each mineral were obtained by processing the μ-XRF map with the software program 'Petromod' (Cossio *et al.*, 2002).

Mineral chemistry

Minerals were analysed using a Cambridge Stereoscan 360 scanning electron microscope (SEM) equipped with an EDS Energy 200 and a Pentafet detector (Oxford Instruments) at the Department of Earth Sciences, University of Torino. The operating conditions were as follows: accelerating voltage was set to 15 kV, beam diameter was 2 μm, and detection limits for oxides were 0·03 wt %. SEM–EDS quantitative data were acquired and
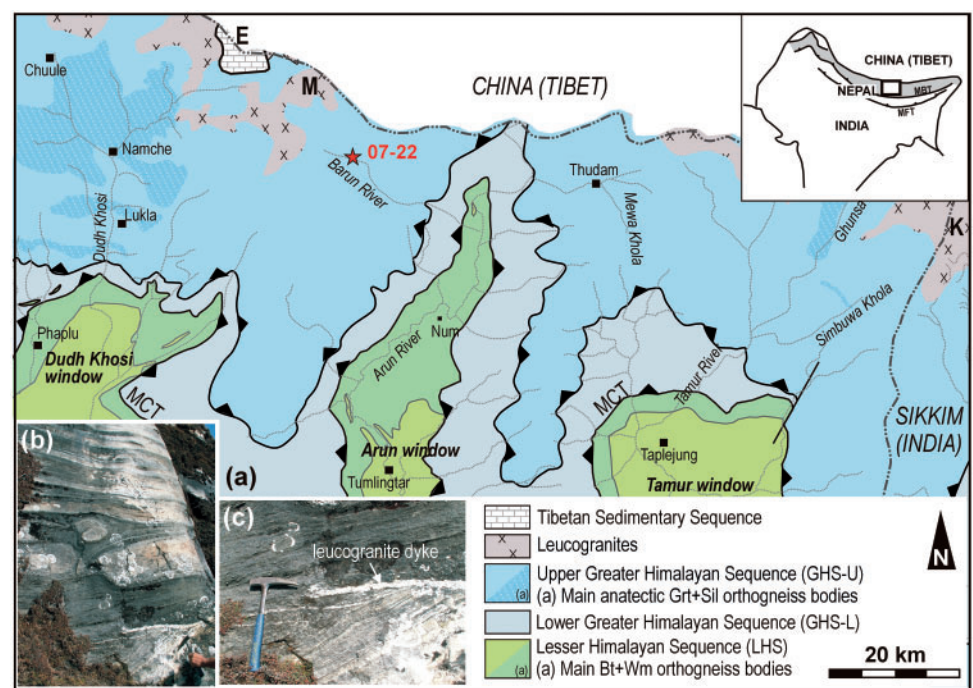
Fig. 1. (a) Simplified geological map of eastern Nepal (modified from Shrestha *et al.*, 1984; Goscombe & Hand, 2000; Goscombe *et al.*, 2006; Mosca *et al.*, 2012) showing the sample location (red star). The dot-dashed line is the approximate political boundary between Nepal to the SW, China (Tibet) to the north and India (Sikkim) to the east. MCT, Main Central Thrust; E, Everest; K, Kangchenjunga; M, Makalu. Inset shows the location of the study area (white rectangle) in the framework of the Himalayan chain. The grey shaded belt approximates the location of the GHS and LHS. MFT, Main Frontal Thrust; MBT, Main Boundary Thrust. (b) Field occurrence of the studied calc-silicate rock, forming a unit tens of meters thick, of more or less boudinaged layers within ana-tectic paragneiss. (c) Detail of (b), showing a leucogranite dyke crosscutting the calc-silicate rock. The peculiar banded structure of the calc-silicate rock is defined by whitish centimeter-sized layers alternating with greenish layers of similar thickness.
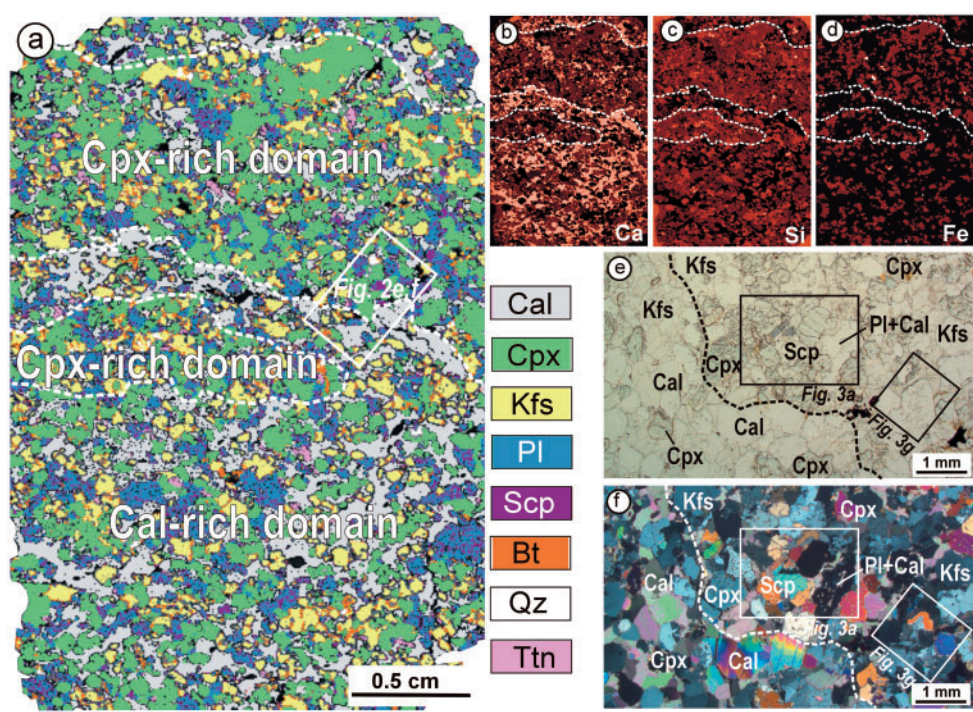
Fig. 2. (a–d) Processed (a) and unprocessed (b: Ca; c: Si; d: Fe) major element μ-XRF map of a whole thin section of sample 07–22, with distinction of the Cpx- and Cal-rich domains. (e, f) Representative microstructures of both Cpx- and Cal-rich domains (upper right and bottom left, respectively) under the optical microscope (e, plane-polarized light, PPL; f, cross-polarized light, XPL).

processed using the Microanalysis Suite Issue 12, INCA Suite version 4.01; natural mineral standards were used to calibrate the raw data; the $\rho\phi Z$ correction (Pouchou & Pichoir, 1988) was applied. The absolute error is 1σ for all calculated oxides. Mineral chemical data for representative minerals are reported in Tables 1 and 2.

Phase diagram computation

Phase diagrams in the NKC(F)MAS(T)-HC system were calculated using Perple_X (version 6·7·2, Connolly, 1990, 2009) and the thermodynamic dataset and equation of state for H_2O–CO_2 fluid of Holland & Powell (1998, revised 2004).

AQ3

Table 1: Representative SEM-EDS analyses of clinopyroxene, K-feldspar and plagioclase in the Cpx-rich (G) and Cal-rich (P) domains

	Clinopyroxene					K-feldspar		Plagioclase							
Analysis:	3.31G porphyroblast	4.6G	2.2G granoblast	11.2P		3.12G In Cpx	5.18P In Zo	6.18G	6.19G	10.3P Lamellar intergrowths	10.4P	3.3G In Cpx	3.23G	5.4P In Zo	8.15P
	core	rim										porphyroblast			
SiO_2	52·32	52·03	51·89	51·10	SiO_2	65·44	65·18	49·83	52·52	50·39	57·68	58·16	60·40	66·26	66·88
TiO_2	b.d.l.	b.d.l.	b.d.l.	b.d.l.	TiO_2	b.d.l.	b.d.l.	b.d.l.	b.d.l.	b.d.l.	b.d.l.	b.d.l.	b.d.l.	b.d.l.	b.d.l.
Al_2O_3	2·01	b.d.l.	0·67	2·60	Al_2O_3	18·20	17·79	31·60	29·60	30·95	26·48	26·51	24·62	21·18	20·89
FeO	9·09	11·25	11·78	11·20	FeO	b.d.l.	b.d.l.	b.d.l.	b.d.l.	b.d.l.	b.d.l.	b.d.l.	b.d.l.	b.d.l.	b.d.l.
MnO	b.d.l.	b.d.l.	b.d.l.	b.d.l.	MnO	b.d.l.	b.d.l.	b.d.l.	b.d.l.	b.d.l.	b.d.l.	b.d.l.	b.d.l.	b.d.l.	b.d.l.
MgO	11·38	11·11	10·61	10·15	MgO	b.d.l.	b.d.l.	b.d.l.	b.d.l.	b.d.l.	b.d.l.	b.d.l.	b.d.l.	b.d.l.	b.d.l.
CaO	24·99	25·44	25·08	24·98	CaO	b.d.l.	b.d.l.	16·40	13·82	15·15	9·81	9·55	8·70	2·69	3·42
Na_2O	0·48	b.d.l.	b.d.l.	0·39	Na_2O	0·63	0·49	2·82	4·04	3·26	6·02	6·05	6·86	9·70	9·36
K_2O	b.d.l.	b.d.l.	b.d.l.	b.d.l.	K_2O	16·64	16·64	b.d.l.	b.d.l.	b.d.l.	b.d.l.	b.d.l.	b.d.l.	b.d.l.	b.d.l.
Total	100·39	99·98	100·13	100·68	Total	100·91	100·10	100·65	99·98	99·75	99·99	100·27	100·58	99·82	100·55
Si	1·957	1·977	1·973	1·925	Si	2·993	3·009	2·263	2·387	2·303	2·597	2·611	2·696	2·935	2·951
Ti	0·000	0·000	0·000	0·000	Ti	0·000	0·000	0·000	0·000	0·000	0·000	0·000	0·000	0·000	0·000
Al	0·089	0·000	0·030	0·115	Al	0·981	0·968	1·691	1·585	1·667	1·405	1·403	1·295	1·105	1·087
Fe^{3+}	0·033	0·045	0·025	0·064	Fe^{3+}	0·000	0·000	0·000	0·000	0·000	0·000	0·000	0·000	0·000	0·000
Fe^{2+}	0·251	0·312	0·350	0·290	Fe^{2+}	0·000	0·000	0·000	0·000	0·000	0·000	0·000	0·000	0·000	0·000
Mn	0·000	0·000	0·000	0·000	Mn	0·000	0·000	0·000	0·000	0·000	0·000	0·000	0·000	0·000	0·000
Mg	0·635	0·629	0·601	0·570	Mg	0·000	0·000	0·000	0·000	0·000	0·000	0·000	0·000	0·000	0·000
Ca	1·001	1·036	1·022	1·008	Ca	0·000	0·000	0·798	0·673	0·742	0·473	0·459	0·416	0·128	0·162
Na	0·035	0·000	0·000	0·029	Na	0·056	0·043	0·248	0·356	0·289	0·526	0·527	0·594	0·833	0·801
K	0·000	0·000	0·000	0·000	K	0·971	0·980	0·000	0·000	0·000	0·000	0·000	0·000	0·000	0·000
X_{Mg}	0·72	0·67	0·63	0·66	Ab	0·05	0·04	0·24	0·35	0·28	0·53	0·53	0·59	0·87	0·83
					An	0·00	0·00	0·76	0·65	0·72	0·47	0·47	0·41	0·13	0·17
					Or	0·95	0·96	0·00	0·00	0·00	0·00	0·00	0·00	0·00	0·00

Structural formulae have been calculated on the basis of 6 oxygens for clinopyroxene and 8 oxygens for K-feldspar and plagioclase. Fe^{3+} has been calculated by stoichiometry. b.d.l., below detection limit.

Table 2: Representative SEM-EDS analyses of scapolite, biotite, muscovite, zoisite and amphibole in the Cpx-rich (G) and Cal-rich (P) domains

	Scapolite						Biotite		Muscovite		Epidote			Amphibole	
Analysis:	6.12G In matrix	11.12P In matrix	7.8G In Cpx	11.19G In Cpx	5.20P In Zo		2.10G In matrix	6.2G In Cpx	11.9P In Zo		8.5P	11.11P		3.9G In Cpx	7.4G In Cpx
SiO_2	45·22	44·60	45·68	44·02	45·58	SiO_2	39·66	38·80	48·96	SiO_2	39·27	39·28	SiO_2	50·59	51·37
TiO_2	b.d.l.	b.d.l.	b.d.l.	b.d.l.	b.d.l.	TiO_2	0·99	2·16	b.d.l.	TiO_2	b.d.l.	b.d.l.	TiO_2	0·52	b.d.l.
Al_2O_3	27·90	27·06	26·58	26·47	27·53	Al_2O_3	15·75	14·48	33·13	Al_2O_3	32·31	30·82	Al_2O_3	5·40	4·26
FeO	b.d.l.	b.d.l.	b.d.l.	b.d.l.	b.d.l.	FeO	17·80	19·12	0·73	FeO	b.d.l.	1·23	FeO	13·57	15·24
MnO	b.d.l.	b.d.l.	b.d.l.	b.d.l.	b.d.l.	MnO	b.d.l.	b.d.l.	b.d.l.	MnO	b.d.l.	b.d.l.	MnO	b.d.l.	b.d.l.
MgO	b.d.l.	b.d.l.	b.d.l.	b.d.l.	b.d.l.	MgO	13·58	11·73	1·24	MgO	b.d.l.	b.d.l.	MgO	13·71	12·90
CaO	20·77	20·84	19·64	21·35	20·13	CaO	b.d.l.	b.d.l.	b.d.l.	CaO	26·36	26·43	CaO	13·52	13·63
Na_2O	2·59	2·48	2·94	2·13	2·72	Na_2O	b.d.l.	b.d.l.	b.d.l.	Na_2O	b.d.l.	b.d.l.	Na_2O	0·64	0·30
K_2O	b.d.l.	b.d.l.	b.d.l.	b.d.l.	b.d.l.	K_2O	8·33	10·10	10·96	K_2O	b.d.l.	b.d.l.	K_2O	b.d.l.	0·40
Cl	b.d.l.	b.d.l.	b.d.l.	b.d.l.	b.d.l.	Total	96·11	96·40	95·02	Total	97·93	97·76	Total	97·97	98·09
Total	96·48	94·98	94·84	93·97	95·96										
Si	6·948	6·997	7·118	7·023	7·010	Si	2·950	2·986	3·247	Si	2·995	3·014	Si	7·323	7·484
Ti	b.d.l.	b.d.l.	0·000	0·000	0·000	Ti	0·055	0·125	0·000	Ti	0·000	0·000	Ti	0·057	0·000
Al	5·052	5·003	4·882	4·977	4·990	Al	1·381	1·313	2·590	Al	2·904	2·787	Al	0·922	0·731
Fe^{3+}	0·000	0·000	0·000	0·000	0·000	Fe^{3+}	0·000	0·000	0·000	Fe^{3+}	0·000	0·080	Fe^{3+}	0·137	0·144
Fe^{2+}	0·000	0·000	0·000	0·000	0·000	Fe^{2+}	1·108	1·230	0·041	Fe^{2+}	0·000	0·000	Fe^{2+}	1·506	1·713
Mn	0·000	0·000	0·000	0·000	0·000	Mn	0·000	0·000	0·000	Mn	0·000	0·000	Mn	0·000	0·000
Mg	0·000	0·000	0·000	0·000	0·000	Mg	1·506	1·346	0·122	Mg	0·000	0·000	Mg	2·959	2·801
Ca	3·419	3·503	3·279	3·649	3·317	Ca	0·000	0·000	0·000	Ca	2·154	2·173	Ca	2·097	2·127
Na	0·772	0·754	0·888	0·659	0·811	Na	0·000	0·000	0·000	Na	0·000	0·000	Na	0·181	0·084
K	0·000	0·000	0·000	0·000	0·000	K	0·791	0·992	0·927	K	0·000	0·000	K	0·000	0·074
CO_2	1·000	1·000	1·000	1·000	1·000										
EqAn	0·68	0·67	0·63	0·66	0·66	X_{Mg}	0·58	0·52	0·75	Zo	0·90	0·79	X_{Mg}	0·66	0·62

Structural formulae have been calculated on the basis of: Si + Al = 12 and CO_2 = 1 – Cl for scapolite; 11 oxygens for biotite and muscovite; 12 oxygens for epidote; 23 oxygens and 15 cations + Na + K for amphibole. Fe^{3+} has been calculated by stoichiometry. b.d.l., below detection limit.

Table 3: Bulk compositions of Cpx- and Cal-rich domains (wt %)

	Cpx-rich domain	Cal-rich domain
SiO_2	48·12	42·62
TiO_2	0·67	0·71
Al_2O_3	12·57	13·82
FeO	4·88	3·49
MgO	5·69	3·85
CaO	24·14	31·22
Na_2O	0·92	0·99
K_2O	3·00	3·30
Total	100·00	100·00

Isobaric T–X(CO₂) grid and mixed-volatile P–T grid

For the calculation of the isobaric $T–X(CO_2)$ grid and mixed-volatile $P–T$ grid in the NKCMAS-HC system, the following solid end-members were considered: calcite, clinochlore, diopside, kyanite, microcline, muscovite, phlogopite, quartz, sillimanite, tremolite and zoisite, in addition to the solution models of plagioclase (Newton et al., 1980) and scapolite (Kuhn, 2005) and to the binary $H_2O–CO_2$ fluid (Connolly & Trommsdorff, 1991). Concerning scapolite, it should be noted that the actually available solid solution model (Kuhn, 2005) does not include S- and Cl-bearing end-members: the Na–Ca substitution is modelled by the three end-members meionite (me: $Ca_3Al_6Si_6O_{24}.CaCO_3$), mizzonite (mizz: $NaCa_2Al_5Si_7O_{24}.CaCO_3$) and CO_3-marialite (coma: $Na_3Al_3Si_9O_{24}.CaCO_3$). Although S and Cl have not been detected in the analysed scapolite (see below), the presence of minor amounts (lower than the detection limit of the EDS detector, i.e. <0·03 wt %) of these elements in scapolite might modify its $a–X$ relations, eventually affecting phase relations in the calculated phase diagrams. However, as far as the modelled phase equilibria are able to explain the observed microstructures and are consistent with the independently constrained $P–T$ evolution of the studied rock, we are confident that the scapolite solution model is meaningful.

Owing to the complexity of the investigated system, the following simplifications are required to reduce the number of equilibria to the most relevant ones

1. The effects of Mg–Fe substitution in mafic minerals have been simulated using reduced activities for diopside, tremolite, clinochlore and phlogopite, matching the measured compositions (i.e. $aDi = 0·7$, $aTr = 0·6$, $aClc = 0·6$, $aPhl = 0·6$). Additional calculations were made using $aDi = 0·8$ and $aPhl = 0·5$, corresponding to the core composition of porphyroblastic clinopyroxene and biotite included in clinopyroxene (see below).
2. Grossular and wollastonite are systematically absent in the studied calc-silicate rocks and in many scapolite-bearing calc-silicate rocks described in the literature (Bucher & Grapes, 2011, and references therein), although some exceptions have been also reported (e.g. Harley & Buick, 1992). They were included in the calculation, but the garnet- and wollastonite-involving reactions are not discussed in detail. The same approach applies for corundum, which has never been observed in these rocks: corundum has been included in the calculation, but the corundum-bearing univariant reactions and invariant points are not shown in the $T–X(CO_2)$ grid. This results in the apparent abrupt termination of those univariant curves that terminate at a Crn-bearing invariant point. Although not elegant, this approach is needed to simplify, from a graphical point of view, the otherwise excessive density of equilibrium curves in the $T–X(CO_2)$ grid.
3. The phase diagram computation was further simplified by neglecting dolomite and margarite. Both dolomite and margarite stability fields, in fact, are limited to relatively low T (e.g. Bucher & Grapes, 2011). Furthermore, these phases do not occur in the studied sample (and, more generally, in most of the scapolite-bearing calc-silicate rocks described in the literature; Bucher & Grapes, 2011, and references therein).

All these simplifications are nevertheless overcome by the modelled $T–X(CO_2)$ pseudosections, which include the effects of Mg–Fe substitution in mafic minerals and also consider those phases that are neglected in the isobaric $T–X(CO_2)$ grid and in the mixed-volatile $P–T$ projection (e.g. garnet, wollastonite, dolomite, margarite, corundum) (see below).

Finally, in contrast to the common practice in calculating isobaric $T–X(CO_2)$ grids, calcite and quartz are not considered as excess phases. These minerals, in fact, mostly behave as reactants during prograde metamorphism and they may be completely consumed at medium to high metamorphic grades. Calcite- and quartz-absent equilibria, potentially relevant for the modelling of calc-silicate assemblages, are therefore considered, thus giving to the modelled $T–X(CO_2)$ grids a more general validity.

Isobaric T–X(CO₂) pseudosections

The bulk-rock compositions of the different layers recognized in the studied sample 07–22 have been calculated by combining the mineral proportions obtained from modal estimates of micro-XRF maps (Fig. 2) with mineral chemistry acquired by SEM–EDS (Tables 1 and 2), and are reported in Table 3.

For the calculation of the isobaric $T–X(CO_2)$ pseudosections in the NKCFMAST-HC system, the following solid solution models were used: amphibole (Diener et al., 2007; Diener & Powell, 2012), biotite (Tajcmanova et al., 2009), chlorite (Holland & Powell, 1998), clinopyroxene (Holland & Powell, 1998), dolomite (Holland & Powell, 1998), garnet (Holland & Powell, 1998), plagioclase (Newton et al., 1980) and scapolite (Kuhn, 2005), in addition to the binary $H_2O–CO_2$ fluid. Calcite, K-feldspar, muscovite, paragonite, margarite, kyanite, quartz and zoisite were considered as pure end-members. In the pseudosection modelling, the binary $H_2O–CO_2$ fluid is considered as a saturated fluid phase.

PETROGRAPHY AND MINERAL CHEMISTRY

The studied sample 07–22 is a fine-grained calc-silicate rock with a granoblastic structure, characterized by clinopyroxene-rich domains alternating with calcite-rich domains, defining a centimetre-thick layering (Figs 2–4). The clinopyroxene- and calcite-rich layers have similar mineral assemblages (Fig. 2e and f) consisting of clinopyroxene + calcite + K-feldspar + plagioclase + scapolite ± zoisite and minor quartz and biotite, but with different modal amounts of the main mineral phases. Mineral abbreviations are from Whitney & Evans (2010).
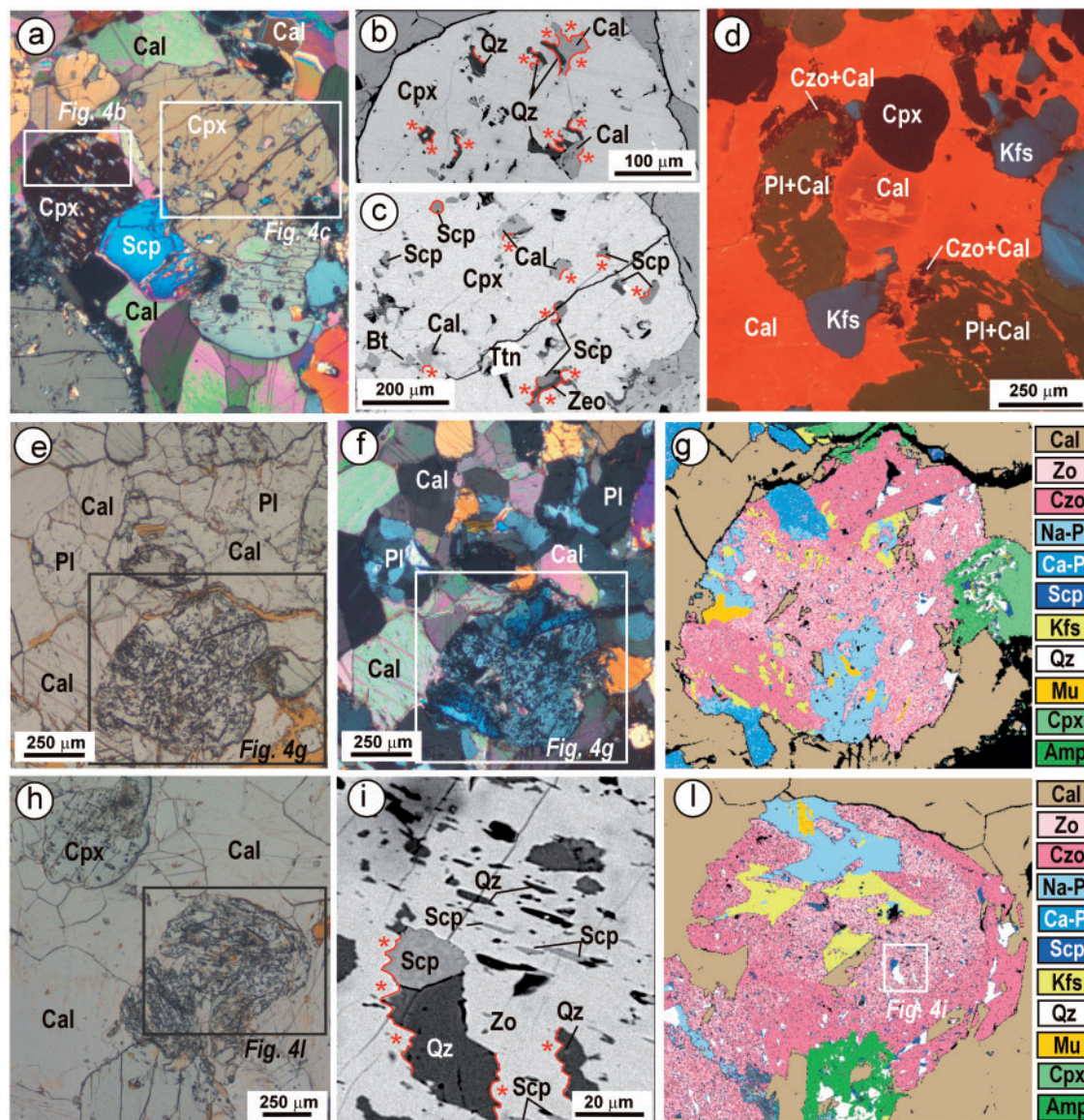
Clinopyroxene-rich domains

The clinopyroxene-rich domains consist of clinopyroxene (39 vol. %), plagioclase (18 vol. %), calcite (15 vol. %), K-feldspar (14 vol. %), scapolite (8 vol. %), minor biotite (4 vol. %) and quartz (1 vol. %), and accessory titanite (1 vol. %) and bluish tourmaline (Fig. 3a and b).

Clinopyroxene mainly occurs as fine-grained granoblasts (Fig. 3a and b), but occasionally forms large porphyroblasts (Fig. 3c). The rare clinopyroxene porphyroblasts are slightly zoned (core: $Di_{70–72}$; rim: $Di_{67–68}$) (Fig. 5a, Table 1). The cores of clinopyroxene porphyroblasts contain small, mono- and polymineralic inclusions of amphibole
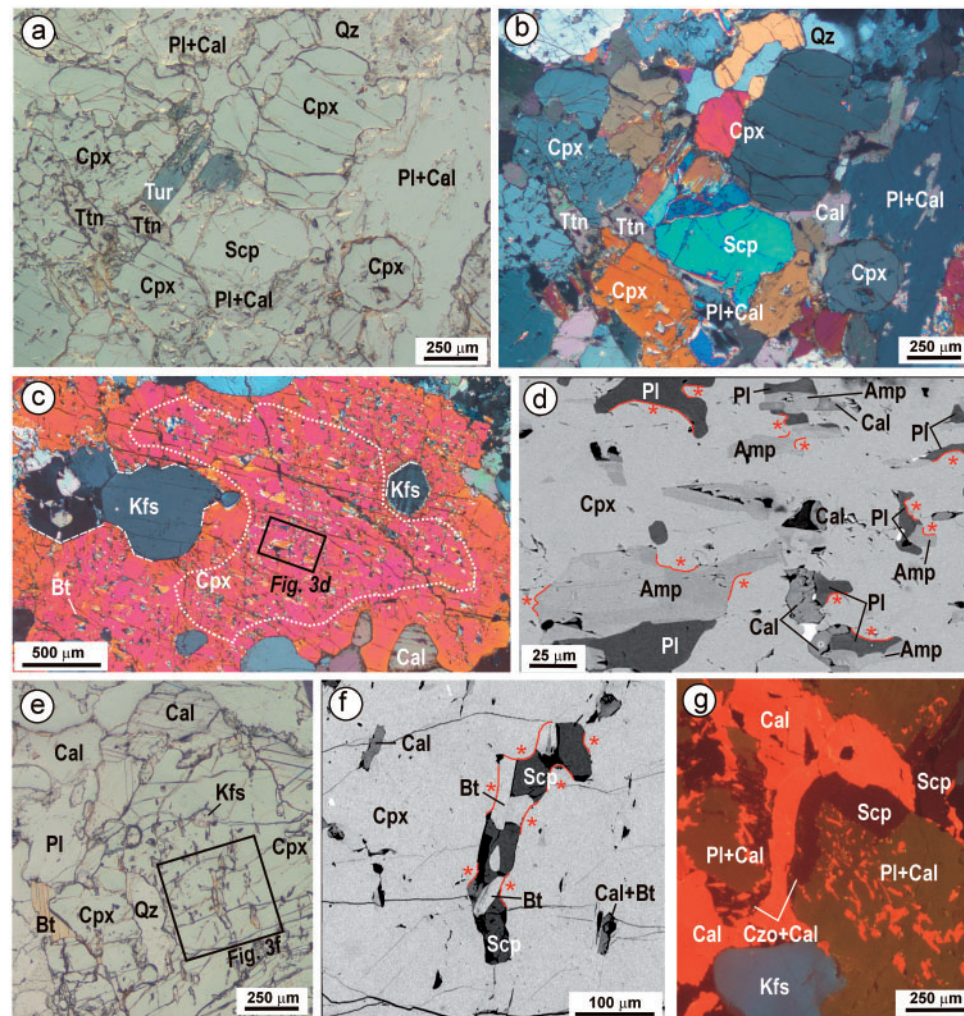
Fig. 3. Representative microstructures of Cpx-rich domains. (a, b) Granoblastic clinopyroxene in equilibrium with scapolite and calcite; plagioclase + calcite aggregates partially or completely replace scapolite. Peculiar bluish tourmaline occurs as an accessory phase (a, PPL; b, XPL). (c) Microstructurally zoned, centimeter-sized clinopyroxene porphyroblast. The core (delimited by the dotted white line) is crowded with plagioclase + amphibole + calcite ± quartz ± zoisite fine-grained inclusions showing corroded and lobate margins against clinopyroxene, whereas the rim includes fine-grained biotite + calcite + quartz and coarse-grained K-feldspar with straight margins against clinopyroxene (dashed white lines) (XPL). (d) Detail of (c), showing polymineralic inclusions (Amp + Pl + Cal) hosted in a porphyroblastic clinopyroxene core. The corroded and lobate margins of the inclusions (red asterisks) should be noted; these suggest 'active' participation of these minerals as reactants in the Cpx-forming reaction [back-scattered electron (BSE) image]. (e) Granoblastic clinopyroxene with oriented fine-grained inclusions of biotite + calcite + scapolite + quartz ± amphibole and coarse-grained inclusions of K-feldspar (PPL). (f) Detail of (e), showing polymineralic inclusions of Bt + Scp + Cal within granoblastic clinopyroxene (BSE image). (g) Plagioclase + calcite symplectitic aggregates growing at the expense of scapolite, still locally preserved. Clinozoisite occurs as discontinuous rims surrounding the Pl + Cal symplectite (CL image).

Fig. 4. Representative microstructures of Cal-rich domains. (a) Granoblastic clinopyroxene in equilibrium with scapolite and calcite (XPL). (b, c) Details of (a) showing calcite + quartz + scapolite + biotite inclusions within clinopyroxene, showing corroded and lobate margins (red asterisks), suggesting 'active' participation of these minerals as reactants in the Cpx-forming reaction (BSE images). (d) Plagioclase + calcite symplectitic aggregates growing at the expense of scapolite, rimmed by clinozoisite + calcite. The slightly darker core of the calcite granoblast, corresponding to a very slight enrichment in Mg, should be noted (CL image). (e, f) Zoisite granoblast with a dusty appearance owing to the high amount of inclusions (fine-grained quartz + scapolite + calcite + muscovite and coarse-grained Na-rich plagioclase + K-feldspar) (e, PPL; f, XPL). (g) Processed X-ray map of zoisite shown in (e), highlighting the distribution of inclusions. (h) Zoisite granoblast with similar microstructural features to that in (e) (PPL). (i) Detail of (h) and (l) showing the fine-grained quartz + scapolite inclusions within zoisite, characterized by corroded and lobate margins (red asterisks) (BSE image). (l) Processed X-ray map of zoisite shown in (h), highlighting the inclusion distribution.

(magnesiohornblende) + plagioclase (An$_{37-60}$; Table 1) + calcite ± quartz ± zoisite ± titanite, showing lobate, rounded and corroded contacts with the host clinopyroxene (Fig. 3d); the rims of the clinopyroxene porphyroblasts include quartz, calcite and biotite with corroded margins, as well as coarse-grained K-feldspar showing straight contacts against clinopyroxene (Fig. 3c) and sporadic fine-grained Ca-rich plagioclase (An$_{80-88}$). The fine-grained granoblasts are homogeneous in composition (Di$_{65-67}$)

(Fig. 5a, Table 1) and contain fine-grained oriented polymineralic inclusions of biotite ($X_{Mg} = 50–56$; Table 2) + scapolite (eqAn$_{61-67}$; Table 2) + calcite ± quartz ± titanite, often showing lobate and rounded contacts with the host clinopyroxene (Fig. 3e and f). Clinopyroxene is locally partially replaced by actinolitic amphibole at its rim.

Scapolite (eqAn$_{66-69}$; Table 2) in the matrix is often partially or completely replaced by symplectitic aggregates of plagioclase + calcite (Fig. 3a, b and g).
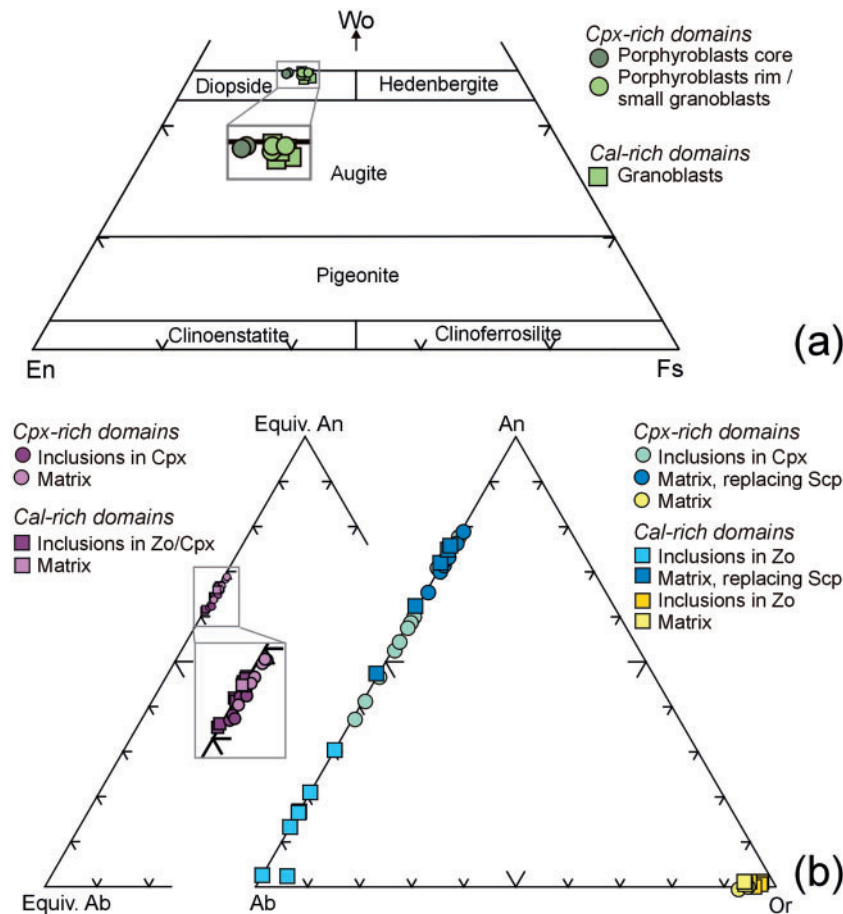
Fig. 5. (a) Clinopyroxene compositions plotted in the En–Fs–Di–Hed diagram. (b) Scapolite, plagioclase and K-feldspar compositions plotted in the eqAb–eqAn diagram and in the Ab–An–Or diagram, respectively.

Plagioclase replacing scapolite is not homogeneous in composition, forming lamellar intergrowths (tens of microns thick) of andesine–labradorite (An_{47-65}) and bytownite (An_{72-80}) (Table 1). These two-phase lamellar intergrowths, which are fairly common in metacarbonate rocks, have been investigated by Grove *et al.* (1983, 1986) and have been interpreted as the result of metastable plagioclase growth and/or decomposition at amphibolite-facies conditions (400–575°C). It has been demonstrated that even the long equilibration times associated with regional metamorphism fail to produce equilibrium plagioclase feldspar compositions [see Grove *et al.* (1983) for further details]. These symplectitic aggregates of plagioclase + calcite are locally surrounded by a discontinuous rim of clinozoisite + calcite (Fig. 3g).

Biotite ($X_{Mg} = 0{\cdot}57$–$0{\cdot}58$; Table 2) occurs as relict flakes in the matrix, overgrown by clinopyroxene (Fig. 3e). K-feldspar (Or_{93-95}) (Fig. 5b, Table 1) and calcite are almost pure in composition.

Calcite-rich domains

The calcite-rich domains consist of calcite (29 vol. %), clinopyroxene (22 vol. %), plagioclase (19 vol. %), K-feldspar (17 vol. %), scapolite (9 vol. %), zoisite (2 vol. %), minor biotite (1 vol. %) and quartz (<1 vol. %), and accessory titanite (1 vol. %) (Fig. 4a).

Calcite is almost pure in composition; rare calcite grains show a slightly darker core in cathodoluminescence (CL) images (Fig. 4d), which is characterized by a very slight enrichment in Mg ($X_{Mg} = 0{\cdot}005$–$0{\cdot}007$). Clinopyroxene forms fine-grained granoblasts similar in composition to those in the clinopyroxene-rich domains (Di_{64-67}; Table 1), and contains oriented polymineralic inclusions of scapolite (eqAn$_{61-67}$) + calcite ± biotite ($X_{Mg} = 0{\cdot}50$–$0{\cdot}56$) ± quartz, showing lobate, rounded and corroded contacts with the host clinopyroxene (Fig. 4a–c).

Scapolite in the matrix has the same composition and microstructural features as in the clinopyroxene-rich domains (i.e. eqAn$_{66-69}$; partially replaced by plagioclase + calcite aggregates; Fig. 4d, Table 2). The rare zoisite grains include very fine-grained quartz, scapolite (eqAn$_{66-67}$; Table 2), muscovite and calcite; coarser-grained Na-rich plagioclase (An_{2-30}; Table 1) and K-feldspar (Or_{95-97}; Table 1) are also included (Fig. 4e–l) and locally show crystal faces against zoisite (Fig. 4g and l), whereas the very fine-grained inclusions generally have rounded and corroded margins (Fig. 4i). Zoisite (Zo_{86-90}; Table 2) is rimmed and/or overgrown by retrograde clinozoisite (Zo_{61-79}).
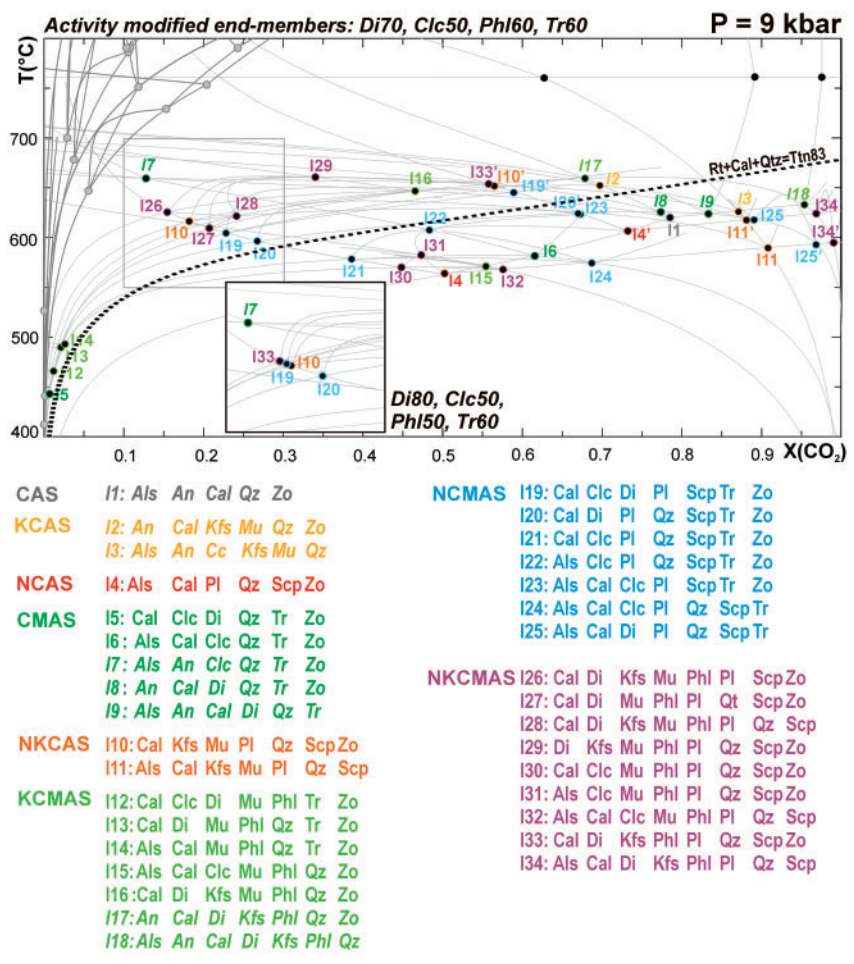
Fig. 6. Isobaric $T–X(CO_2)$ phase diagram in the system NKCMAS(T)-HC at a pressure of 9 kbar, calculated for aDi $= 0.7$, aClc $= 0.5$, aPhl $= 0.6$, aTr $= 0.6$, and for aDi $= 0.8$, aClc $= 0.5$, aPhl $= 0.5$, aTr $= 0.6$ (corresponding to the core composition of porphyroblastic clinopyroxene and to biotite included in clinopyroxene; in the inset). Undifferentiated isobaric univariant curves are shown as fine grey lines. Large filled points with colored labels are isobaric invariant points: each color refers to a specific subsystem (as listed in the legend). The decarbonation equilibrium Rt + Cal + Qz = Ttn, calculated at aTtn $= 0.83$, is also shown by dashed black line.

RESULTS

$T–X(CO_2)$ grid in the system NKCMAS-HC
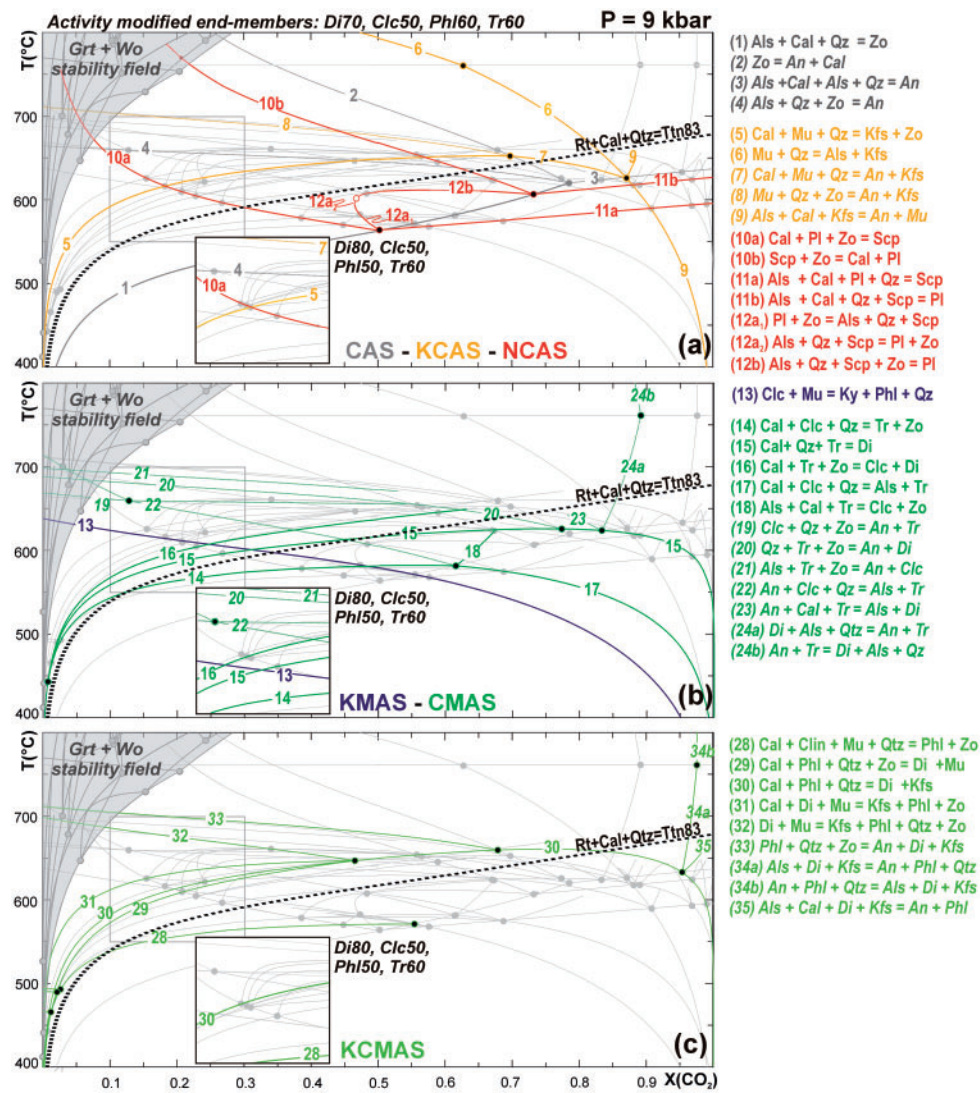
Microstructural sites containing clinopyroxene and zoisite are the most useful to reconstruct the $P–T–X_{fluid}$ evolution of the studied calc-silicate rock. Both hydrous phases and calcite are included in clinopyroxene and zoisite, and microstructural evidence suggests that these inclusions have been consumed during the clinopyroxene and zoisite formation. Therefore, the prograde growth of clinopyroxene and zoisite could have triggered the prograde release of a CO_2-rich fluid.

To investigate the clinopyroxene- and zoisite-forming reactions, an isobaric $T–X(CO_2)$ grid in the fluid-saturated NKCMAS-HC model system was calculated at 9 kbar (Figs 6 and 7); that is, at a pressure compatible with the tightly constrained, nearly isobaric, prograde metamorphic evolution of the associated lithologies (Groppo *et al.*, 2012), considering the plagioclase and scapolite solid solutions and reduced activities for diopside, tremolite, clinochlore and phlogopite as discussed above.

The eight-component NKCMAS-HC system may be described in terms of several subsystems: one five-component subsystem (CAS-HC), four six-component subsystems (KCAS-HC, NCAS-HC, CMAS-HC, KMAS-HC) and three seven-component subsystems (NKCAS-HC, KCMAS-HC, NCMAS-HC).

The CAS-HC, KCAS-HC, KMAS-HC, CMAS-HC and KCMAS-HC subsystems

The CAS-HC, KCAS-HC, CMAS-HC and KCMAS-HC subsystems do not involve Na–Ca solid solutions (plagioclase and scapolite). Several isobaric invariant points occur in these subsystems (I1: CAS-HC; I2–I3: KCAS-HC; I5–I9: CMAS-HC; I12–I18: KCMAS-HC) and are reported in Fig. 6. Invariant points involving the pure anorthite end-member (An_{100}) of the plagioclase solid solution, kyanite and/or chlorite are not relevant for this study, because these phases have not been observed in the studied sample. Therefore, the two most relevant invariant points in these subsystems are I13 and I16 (KCMAS-HC subsystem).

J_ID: **PETROLOGY** Customer A_ID: **EGX005** Copyedited by: **PR** Manuscript Category: **Original Article** Cadmus Art: **O**

NOT FOR PUBLIC RELEASE

Journal of Petrology, 2017, Vol. 0, No. 0   **11**

Fig. 7. Same isobaric $T–X(CO_2)$ phase diagram as in Fig. 6. Isobaric univariant reactions are represented separately and with different colors for each subsystem. Large filled points with colored outline are isobaric invariant points as in Fig. 6. Small open points are singular points. Equilibrium curves reported as dotted lines (in italic in the legend) involve the pure anorthite end-member of the plagioclase solid solution (An_{100}). The decarbonation equilibrium $Rt + Cal + Qz = Ttn$, calculated at $aTtn = 0.83$, is shown as a dashed black line. The shaded area indicates the garnet + wollastonite stability field (Grt- and Wo-bearing equilibria are shown as undifferentiated grey lines). Reactions are written such as the products are on the high-T side of the equilibrium curves.

Reaction equilibria in these subsystems are reported in Fig. 7a–c and have been widely discussed by many researchers (e.g. Kerrick, 1974; Ferry, 1983b; Bucher & Grapes, 2011, for a review). Most of these equilibria are dehydration or decarbonation equilibria, and are therefore concave downward. A few hydration or decarbonation equilibria (1 and 18) and a few dehydration equilibria (6, 13 and 32) are also present. The latter (equilibria 6, 13 and 32) are calcite-absent equilibria, therefore they are not relevant for the purposes of this study (i.e. the investigation of CO_2-producing processes). Quartz-absent equilibria (16, 18 and 31) are instead potentially relevant for the studied sample, because quartz is present in very low amounts in both domains.

The following isobaric univariant equilibria are relevant for calcite + quartz-bearing systems:

1. zoisite is stable between the CAS-HC equilibria 1 (Als + Cal + Qz = Zo) and 2 (Zo = An + Cal); that is, up to relatively high $X(CO_2)$ values;
2. muscovite is stable below the KCAS-HC equilibrium 5 (Cal + Mu + Qz = Kfs + Zo);
3. chlorite is stable below the CMAS-HC equilibria 14 (Cal + Clc + Qz = Tr + Zo) and 17 (Cal + Clc + Qz = Als + Tr);
4. diopside is stable above the CMAS-HC equilibrium 15 (Cal + Qz + Tr = Di), which also represents the tremolite-out curve;
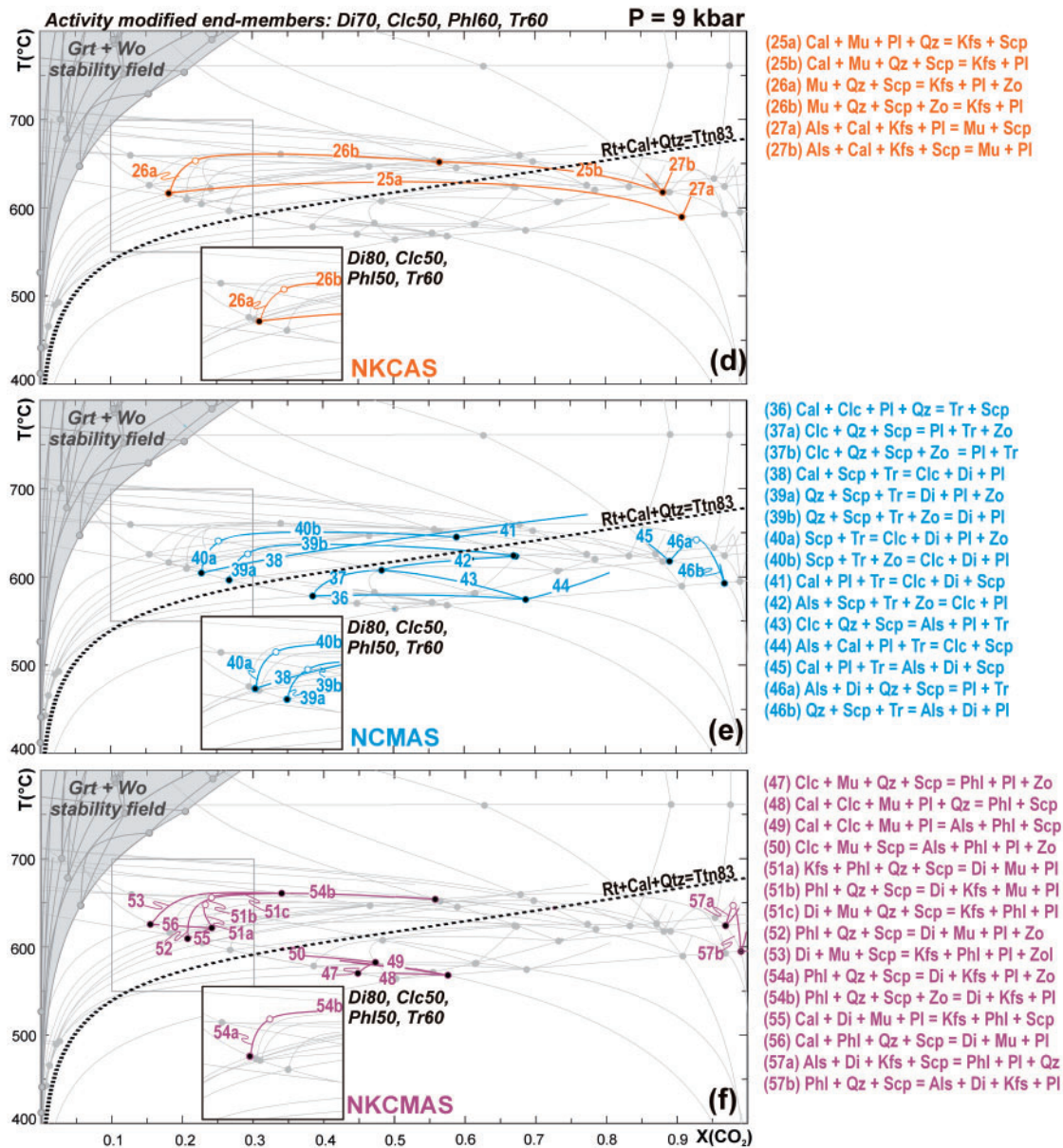
Fig. 7. Continued

5. K-feldspar is stable above the KCMAS-HC equilibrium 30 (Cal + Phl + Qz = Di + Kfs);

6. phlogopite is stable above the KCMAS-HC equilibrium 28 (Cal + Clc + Mu + Qz = Phl + Zo).

Equilibria reported in italics in Fig. 7a–c (dotted lines) involve the pure anorthite end-member of the plagioclase solid solution (An_{100}) and will be discussed further below.

The addition of TiO_2 to the simple CAS-HC subsystem leads to the stabilization of titanite vs rutile, according to the decarbonation equilibrium Rt + Cal + Qz = Ttn. This equilibrium has been calculated considering a reduced activity for titanite (aTtn = 0·83) to match its measured composition, and it is reported in Figs 6 and 7 as a dotted black line. This equilibrium is particularly important for the studied sample; the systematic lack of rutile, in fact, limits the isobaric univariant equilibria (and isobaric invariant points) relevant to this study to those lying above the Ttn-in reaction curve.

It is worth remembering that, without considering the Na–Ca solid solutions (plagioclase and scapolite), these CAS-HC, KCAS-HC, KMAS-HC, CMAS-HC and KCMAS-HC equilibria are the only ones that are predicted in the *P–T* range of interest (Supplementary Data Fig. SM1; supplementary data are available for downloading at http://www.petrology.oxfordjournals.org) (note that the CAS-HC equilibrium An + Cal = Me occurs at $T > 800°$C, at $P = 9$ kbar). It is evident that these equilibria are not sufficient to explain the scapolite-bearing

microstructures observed in the studied sample. This underlines the importance of considering Na–Ca solid solutions in the modelling of scapolite-bearing calc-silicate rocks.

The NCAS-HC subsystem

The NCAS-HC subsystem involves plagioclase and scapolite solid solutions in addition to zoisite, calcite, quartz and kyanite. Three equilibria (10, 11 and 12) describe the topological relationships between plagioclase, scapolite and zoisite; they originate from two isobaric invariant points, resulting from the duplication of the same invariant point I4 (Fig. 6). This topology is in agreement with that proposed by Kuhn (2005).

The degenerate equilibria 10a and 10b (Fig. 7a) involve calcite, zoisite, plagioclase and scapolite, with plagioclase and scapolite changing composition (and therefore stoichiometric coefficients) along the reaction curves. In detail, Na-rich plagioclase (An_{34}) reacts to form scapolite (Me_{59-66}) with increasing temperature (equilibrium 10a: $Cal + Pl + Zo = Scp$), and at slightly higher temperatures scapolite (Me_{66-79}) and zoisite react to form Ca-rich plagioclase (An_{90}) (equilibrium 10b: $Scp + Zo = Cal + Pl$). Similarly, Na-rich plagioclase is consumed along equilibrium 11a ($Cal + Ky + Pl + Qz = Scp$) with increasing temperature, whereas a Ca-rich plagioclase is produced along equilibrium 11b ($Cal + Ky + Qz + Scp = Pl$).

Equilibrium 12 (Fig. 7) is Cal-absent; it is divided in two portions by a singular point at which the stoichiometric coefficient of zoisite becomes zero (12a: $Als + Qz + Scp = Pl + Zo$; 12b: $Als + Qz + Scp + Zo = Pl$). The plagioclase composition changes continuously along this equilibrium curve, with the Ca-richer compositions toward higher T (i.e. from An_{34} at I4 to An_{90} at I4').

The CAS-HC univariant equilibria 2, 3 and 4 (in italics in Fig. 7) are tangential to the equilibrium curves 10, 11 and 12 respectively, at the singular points with the extreme plagioclase composition An_{100} (outside the P–T range of interest). Therefore, equilibria 2, 3 and 4 represent the singular curves conjugate to equilibria 10, 11 and 12 (Abart *et al.*, 1992).

The NKCAS-HC subsystem

The topological relations between plagioclase, scapolite, zoisite, calcite, quartz, kyanite and the K-bearing phases muscovite and K-feldspar are described in this subsystem. Three reactions originate from four isobaric invariant points, resulting from the duplication of the invariant points I10 and I11 (Fig. 6).

Equilibria 25a and 25b (Fig. 7d) involve calcite, quartz, plagioclase, scapolite, muscovite and K-feldspar, with plagioclase and scapolite changing composition along the equilibrium curves. In more detail, Na-rich plagioclase (An_{34}) reacts to form scapolite (Me_{62} to Me_{66} from I10 to I11) with increasing temperature (equilibrium 25a: $Cal + Mu + Pl + Qz = Kfs + Scp$); at slightly higher temperatures, scapolite (Me_{69} to Me_{66} from I10'

to I11') $+$ calcite $+$ muscovite $+$ quartz react to form Ca-rich plagioclase (An_{90}) (equilibrium 25b: $Cal + Mu + Qz + Scp = Kfs + Pl$). Similarly, Na-rich plagioclase is consumed along equilibrium 27a ($Als + Cal + Kfs + Pl = Mu + Scp$) with increasing temperature, whereas a Ca-rich plagioclase is produced along equilibrium 27b ($Als + Cal + Kfs + Scp = Mu + Pl$).

Equilibrium 26 (Fig. 7d) is Cal-absent; it is divided in two portions by a singular point at which the coefficient of zoisite becomes zero (26a: $Mu + Qz + Scp = Kfs + Pl + Zo$; 26b: $Mu + Qz + Scp + Zo = Kfs + Pl$). The plagioclase composition continuously changes along this equilibrium curve, with the Ca-richer compositions toward the higher-T side (i.e. from An_{34} at I10 to An_{90} at I10').

The KCAS-HC univariant equilibria 7, 8 and 9 (in italics in Fig. 7a) are tangential to the equilibrium curves 25, 26 and 27 respectively, at the singular points with the extreme plagioclase composition An_{100} (i.e. they are the singular curves conjugate to equilibria 25, 26 and 27).

The NCMAS-HC subsystem

This subsystem describes the topological relations between plagioclase, scapolite, zoisite, calcite, quartz, kyanite and the Mg-bearing phases chlorite, amphibole and clinopyroxene. Eleven equilibria originate from seven isobaric invariant points (three of them are duplicated; I19, I20 and I25) (Fig. 6). Invariant points I19, I20 and I21 are shifted toward slightly higher T [and lower $X(CO_2)$] if the composition of the core of the clinopyroxene porphyroblasts and of biotite included in clinopyroxene are considered (inset calculated at $aDi = 0.80$ and $aPhl = 0.50$); however, their relative position with respect to I10 does not change. I20 is the only NCMAS-HC isobaric invariant point relevant for this study, because the others involve chlorite and/or kyanite, which are not observed in the studied sample.

The most relevant equilibrium in this subsystem is equilibrium 36 ($Cal + Clc + Pl + Qz = Tr + Scp$), which represents the chlorite-out curve in calcite $+$ quartz-bearing systems (Fig. 7e). Six equilibria (37, 39, 40, 42, 43 and 46) are Cal-absent and will not be discussed in detail, because they are not relevant for the studied sample. Some of them have a singular point at which the stoichiometric coefficient of zoisite becomes zero. Along these curves, plagioclase becomes progressively richer in Ca at increasing $X(CO_2)$ values (e.g. along equilibrium 40 from I19 to I19'). The remaining four equilibria (38, 41, 44 and 45) are Qz-absent.

The CMAS-HC univariant equilibria 19–24 (in italics in Fig. 7b) are tangential to the equilibrium curves 37, 39, 42, 43, 45 and 46, respectively, at the singular points with the extreme plagioclase composition An_{100} (i.e. they are the singular curves conjugate to these equilibria).

The NKCMAS-HC full system

In the full system NKCMAS-HC, up to nine isobaric invariant points occur at the P–T conditions of interest

and some of them are duplicated (e.g. I33 and I34) (Fig. 6). Invariant points I29–I32 and I34 are not relevant for this study because they involve chlorite and/or kyanite, which are not observed in the studied sample. The chlorite and kyanite-absent invariant point I33 ([Mu]; plagioclase and scapolite composition: An_{34}, Me_{62}) occurs in the $T–X(CO_2)$ grid calculated at $aDi = 0.8$ and $aPhl = 0.5$, at an $X(CO_2)$ value slightly lower than the position of I10, and it is duplicated at higher $X(CO_2)$ values (I33′: [Mu]; plagioclase and scapolite composition: An_{90}, Me_{69}). Changing the clinopyroxene and biotite activities to $aDi = 0.7$ and $aPhl = 0.6$ has a dramatic effect on the stability of invariant point I33, which is no longer stable and is replaced by four complementary invariant points: I26 <AQz/>, I27 [Kfs], I28 [Zo] and I29 [Cal] (Fig. 6).

As a consequence, the topology of the univariant curves that originate from these invariant points is different in the two $T–X(CO_2)$ grids (Fig. 7f). In the first case, a Cal-absent equilibrium (equilibrium 54) connects the invariant points I33 and I33′; along this curve, a singular point occurs and plagioclase changes composition from An_{34} at I33 to An_{90} at I33′. In the second case, six NKCMAS-HC univariant curves originate from invariant points I26–I29: among them only equilibria 55 ($Cal + Di + Mu + Pl = Kfs + Phl + Scp$) and 56 ($Cal + Phl + Qz + Scp = Di + Mu + Pl$) involve calcite and are therefore relevant for this study.

$T–X(CO_2)$ pseudosections in the system NKCFMAST-HC

At the $P–T$ conditions of interest, the assemblages and microstructures of calc-silicate rocks are controlled by their bulk compositions. It is therefore to be expected that, in the studied sample, the Cpx- and Cal-rich domains may deviate to some extent in their reaction history during their prograde evolution. Chemographies are conventionally used to show the influence of bulk composition on the progress of the reactions. However, in the case of very complex systems such as the eight-component NKCMAS-HC system, chemographies are difficult to use unless making important simplifications (e.g. considering some phases in excess).

To understand which reactions affected each domain in the studied sample, we have therefore calculated two $T–X(CO_2)$ pseudosections in the 10-component NKCFMAST-HC system using the bulk compositions of the Cpx- and Cal-rich domains, respectively (Table 3). The addition of the FeO component implies that the isobaric univariant equilibria and invariant points discussed above for the FeO-free subsystems and involving Fe–Mg solid solutions become narrow isobaric divariant fields and univariant lines, respectively, in the $T–X(CO_2)$ pseudosections. The addition of TiO_2 allows prediction of the stability field of Ti-phases (i.e. rutile, titanite and ilmenite) in both the Cpx- and Cal-rich domains and accounts for the effects of Ti substitution in biotite.

The resulting $T–X(CO_2)$ pseudosections (Fig. 8) show that Cpx- and Cal-rich domains are sensitive to different reactions. Both domains are sensitive to the NCAS-HC reaction 10, which controls the relative stability of Na- and Ca-rich plagioclase, scapolite and zoisite, as well as the KCMAS-HC reaction 30 (K-feldspar-in or clinopyroxene-in, in Cpx- and Cal-rich domains, respectively). Moreover, the Cpx-rich domain is sensitive to the CMAS-HC reaction 15, which controls the relative stability of the Fe–Mg minerals tremolite and diopside, whereas the Cal-rich domain is sensitive to the KCAS-HC reaction 5 (muscovite-out and K-feldspar-in). As a consequence, each domain is sensitive to different isobaric invariant points and can, therefore, produce different isobaric invariant assemblages. Because in the studied sample rutile is not observed, even as an inclusion, and titanite is abundant, the relevant isobaric invariant points are those located above (i.e. at higher T than) the $Rt + Cal + Qz = Ttn$ reaction curve, namely:

1. I20 (NCMAS-HC) and the duplicated I33 (NKCMAS-HC) invariant points for the Cpx-rich domain;
2. the duplicated I10 (NKCAS-HC) and I33 (NKCMAS-HC) invariant points for the Cal-rich domain.

These isobaric invariant points are located in dolomite- and garnet-free fields (Fig. 8b and d), in agreement with the lack of dolomite and garnet in the studied sample.

Mixed-volatile $P–T$ projection in the system NKC(F)MAS-HC

Mixed-volatile phase diagram projections, in which the volatile composition of the system is projected onto the $P–T$ coordinate frame, are a good expedient for simultaneously considering the effects of the three variables P, T and X^{fluid} on phase relations in the NKC(F)MAS-HC system. Because fluid-present univariant curves in a mixed-volatile $P–T$ projection correspond to invariant points in the corresponding isobaric $T–X(CO_2)$ sections (Baker *et al.*, 1991; Carmichael, 1991; Connolly & Trommsdorff, 1991), mixed-volatile $P–T$ projections are particular useful to discuss the formation of isobaric invariant assemblages.

To simplify, only the fluid-present univariant curves relevant at 9 kbar have been reported in the $P–T$ projection calculated for the system NKC(F)MAS-HC (Fig. 9). These truly univariant curves (U1 to U34) thus correspond to the isobaric invariant points (I1 to I34) discussed above and reported in Fig. 6 (except for those involving the plagioclase end-member An_{100}, which have not been considered). Along each univariant curve, fluid, plagioclase and scapolite may change their compositions; in particular, the $X(CO_2)$ of the fluid increases at increasing pressure. Most of these univariant curves are also characterized by one or more singular points, at which the stoichiometric coefficient of one or more phases becomes zero. These singular points divide each univariant curve in two or more portions, characterized by the same univariant assemblage but by different reactants and products.
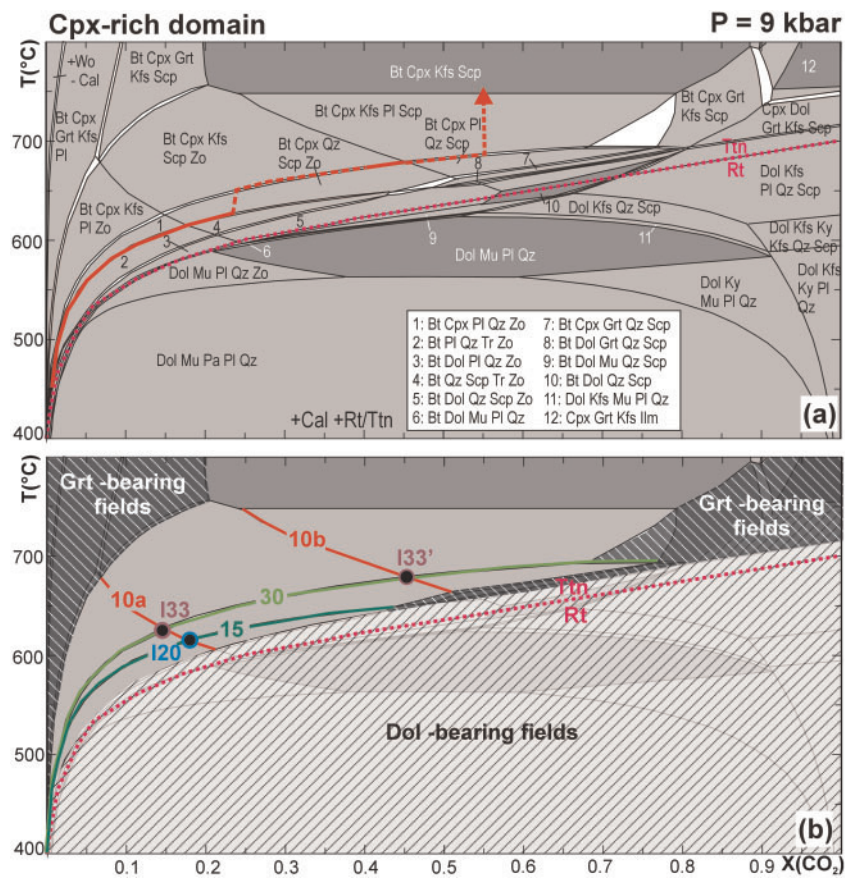
Fig. 8. (a, c) $T–X(CO_2)$ pseudosections calculated for the Cpx-rich (a) and Cal-rich (c) domains, respectively, in the system NKCMFAS-HC at a pressure of 9 kbar. White, light grey and dark grey fields are di-, tri- and quadrivariant fields, respectively. The narrow, isobaric, divariant fields correspond to the isobaric univariant reactions in the corresponding $T–X(CO_2)$ sections. The red arrows approximate the $T–X(CO_2)$ internally buffered fluid evolution as constrained by the relevant microstructures in each domain (dashed portions are more uncertain). (b, d) Same isobaric $T–X(CO_2)$ pseudosections as in (a) and (c): the isobaric univariant and invariant equilibria relevant to Cpx-rich (b) and Cal-rich (d) domains are indicated (reaction labels and colors as in Fig. 7). It should be noted that the univariant curves and invariant points overlap the divariant fields and univariant lines of the pseudosections. The modeled mineral modes and compositions for both Cpx- and Cal-rich domains are reported in Figs 12 and 13, and Supplementary Data SM3.

The relative position of the mixed-volatile truly univariant curves with respect to the $P–T$ evolution inferred from the anatectic paragneiss associated with the studied calc-silicate rock is shown in Fig. 9. All the univariant equilibria are located at $T < 650°C$; that is, they are crossed during the prograde evolution, some 100–150°C lower than peak metamorphic conditions. This has two important consequences: (1) once these univariant curves have been crossed, the studied NKC(F)MAS(T)-HC system is no longer reactive; nothing happens at $T > 650°C$ and the final peak assemblage consists of $Cal + Cpx + Kfs + Scp + Bt \pm Ca$-rich Pl (Fig. 8); (2) CO_2-rich fluids were released through these univariant reactions during the prograde evolution of the studied rock (i.e. prior to peak conditions), at temperatures lower than the muscovite dehydration melting in the associated paragneiss.

The $T–X(CO_2)$ grids and pseudo-sections discussed above allow recognition of the only isobaric invariant points relevant for the Cpx- and Cal-rich domains (I20 and I33' for Cpx-rich domains; I10, I10' and I33' for Cal-rich domains). The corresponding mixed-volatile, truly univariant equilibria U10, U20 and U33 are shown in Fig. 10, with details of the fluid composition. The first univariant curve crossed during the prograde evolution by the Cpx-rich domains is the Cpx-forming reaction U20a $(Cal + Pl + Qz + Tr + Zo \rightarrow Di + Scp + F)$. This reaction is crossed at about 590°C and releases a fluid relatively rich in CO_2 $[X(CO_2) \approx 0.23]$. At higher T (c. 650°C), the Cpx- and Kfs-forming reaction U33c $(Cal + Phl + Qz + Scp + Zo \rightarrow Di + Kfs + Pl + F)$ is crossed, producing a fluid markedly richer in CO_2 $[X(CO_2) \approx 0.52]$. Concerning the Cal-rich domains, both the Zo- and Kfs-producing reaction U10d $(Qz + Cal + Mu + Scp \rightarrow Zo + Pl + Kfs + F)$ and the Cpx- and Kfs-producing reaction U33c $(Cal + Phl + Qz + Scp + Zo \rightarrow Di + Kfs + Pl + F)$ are crossed at c. 650°C, both releasing a CO_2-rich fluid $[X(CO_2) \approx 0.52]$. It is again worth remembering that these truly univariant reactions cannot

J_ID: **PETROLOGY**   Customer A_ID: **EGX005**   Copyedited by: **PR**   Manuscript Category: **Original Article**   Cadmus Art: **O**
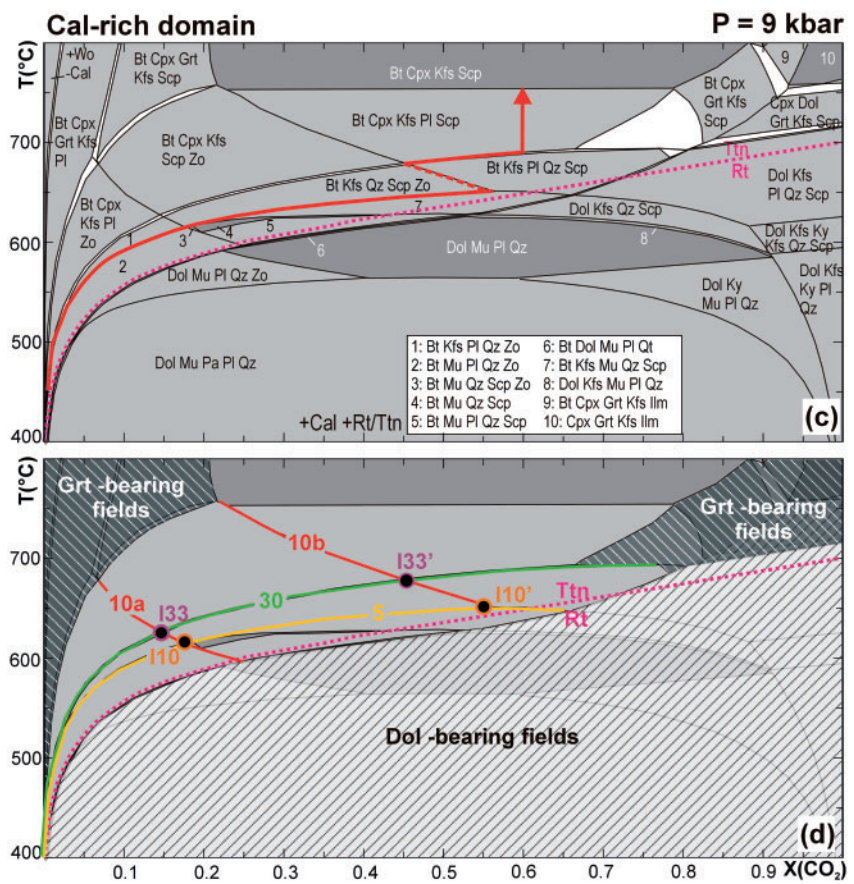
**NOT FOR PUBLIC RELEASE**

Fig. 8. Continued

be recognized without considering Na–Ca solid solutions in the modelling (see Supplementary Data Fig. SM2).

DISCUSSION

Novelty of the proposed 'phase diagram' approach

Thus far, few studies have attempted the thermo-dynamic modelling of metacarbonate rocks in model systems characterized by more than six components. Hewitt (1973) first proposed a simplified $T–X(CO_2)$ grid for the seven-component KCMAS-HC model system to constrain the $P–T–X_{fluid}$ evolution of micaceous lime-stones from south–central Connecticut. One year later, in his review of metamorphic mixed volatile equilibria, Kerrick (1974) presented a simplified $T–X(CO_2)$ grid for the same system, based on experimental data. Ferry (1976) widely discussed the topology of $T–X(CO_2)$ grids for low- and high-grade assemblages in the KCMAS-HC system, and suggested the possible quantitative inad-equacies of $T–X(CO_2)$ diagrams constructed for phases of fixed composition. Following these pioneering works, the progressive improvement of the thermo-dynamic datasets of mineral end-members and the de-velopment of software for thermodynamic modelling (e.g. de Capitani & Brown, 1987; Connolly, 1990, 2009; Powell et al., 1998; de Capitani & Petrakakis, 2010) allowed the calculation of quantitative, rather than qualitative, $T–X(CO_2)$ diagrams in complex model sys-tems (e.g. Cartwright & Buick, 1995: KCMAS-HC sys-tem). Furthermore, the phase equilibria modelling of metacarbonate rocks was significantly improved thanks to the possibility of considering in the calculation both fluid and mineral phases of variable compositions. The resulting mixed-volatile $P–T$ projections (e.g. Baker et al., 1991; Carmichael, 1991; Connolly & Trommsdorff, 1991) allow prediction of the changes in both fluid and mineral compositions as a function of pressure and temperature. This approach has been widely applied in the five- and six-component systems CMS-HC (Skippen, 1971, 1974; Skippen & Hutcheon, 1974; Baker et al., 1991), CAS-HC (Harley & Buick, 1992; Dasgupta, 1993; Fitzsimons & Harley, 1994; Bhowmik et al., 1995; Cartwright et al., 1997; Sengupta et al., 1997; Stephenson & Cook, 1997; Mathavan & Fernando, 2001), CMAS-HC (Carmichael, 1991; Connolly & Trommsdorff, 1991; Schmädicke et al., 2001; Castelli et al., 2007; Groppo et al., 2007), CFAS-C (Robinson, 1991; Sengupta & Raith, 2002) and CFAS-HC (Groppo et al., 2013b), whereas systems with more than six com-ponents have been very little investigated so far (Omori
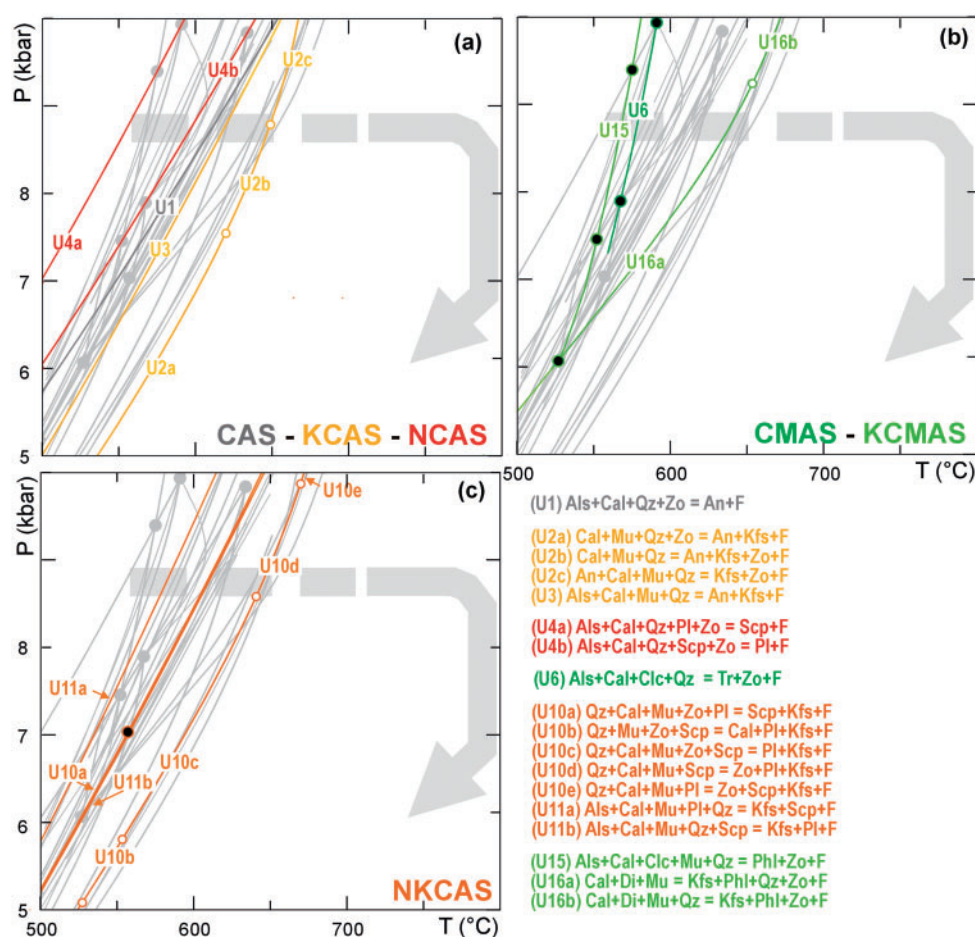
Fig. 9. Mixed-volatile *P–T* projections in the system NKCMAS-HC calculated for $aDi = 0.7$, $aClc = 0.5$, $aPhl = 0.6$ and $aTr = 0.6$. Only the fluid-present univariant curves relevant at 9 kbar are shown. The truly univariant reactions are represented separately and with different colors for each subsystem (yellow, KCAS; red, NCAS; dark green, CMAS; orange, NKCAS; light green, KCMAS; light blue, NCMAS; purple, NKCMAS). Large filled points are true-invariant points; small open points are singular points. The *P–T* evolution inferred from the host anatectic paragneiss (Groppo *et al.*, 2012) is shown by the grey arrow.

et al., 1998: NCMAS-HC and KCMAS-HC systems; Nabelek, 2002: KCFMAS-HC system; López Sánchez Vizcaíno *et al.*, 1997: NKCFMAST-COH graphite-saturated system).

Moreover, in previous calculations the effects of Na–Ca substitution were mostly neglected, although Na–Ca solid solutions (plagioclase and scapolite) are often common in calc-silicate rocks. Owing to the lack of an appropriate solid solution model for scapolite, when considered, the effects of Na–Ca substitution have been generally approximated either using activity-modified end-members (e.g. Harley & Buick, 1992; Dasgupta, 1993; Fitzsimons & Harley, 1994; Bhowmik *et al.*, 1995; Cartwright *et al.*, 1997; Sengupta *et al.*, 1997; Stephenson & Cook, 1997; Satish Kumar & Harley, 1998; Mathavan & Fernando, 2001; Nabelek, 2002), or involving both Na and Ca end-members in the modelled reactions (e.g. Ferry, 1983*a*, 1994; Leger & Ferry, 1993; Ague & Rye, 1999; Ague, 2002, 2003; Ferry *et al.*, 2013). Kuhn (2005) proposed a solution model for scapolite and discussed for the first time phase relations in calc-silicate rocks of a specific bulk-rock composition [i.e. isobaric *T–X*(CO_2) pseudosections: Kuhn *et al.*, 2005] in the nine-component NKCFMAS-HC system, with excess quartz and calcite. A few years later, a similar approach [i.e. *T–X*(CO_2) pseudo-sections in the nine-component NKCFMAS-HC system] was applied by Cottle *et al.* (2011) on calc-silicate rocks from the Himalayas; however, the scapolite solution model was not included in their calculations. Therefore, the work of Kuhn *et al.* (2005) remains so far the only example of petrological investigation of scapolite-bearing rocks in such complex systems.

Starting from the above studies, we have explored the possibility of modelling the scapolite-bearing equilibria relevant for the production of metamorphic CO_2 in calc-silicate rocks belonging to the 10-component system NKCFMAST-HC. Our approach shows three main novelties with respect to previous studies.

1. It combines different types of phase diagrams, each one useful to investigate different aspects of the CO_2-producing history. Specifically: (a) isobaric *T–X*(CO_2) pseudosections allow the recognition of

Fig. 9. Continued

(U19a) Cal+Pl+Tr+Zo = Clc Di Scp F
(U19b) Scp+Tr+Zo = Cal+Clc+Di+Pl+F
(U19c) Cal+Scp+Tr+Zo = Clc+Di+Pl+F
(U20a) Cal+Pl+Qz+Tr+Zo = Di+Scp+F
(U20b) Qz+Scp+Tr+Zo = Cal+Di+Pl+F
(U20c) Cal+Qz+Scp+Tr+Zo = Di+Pl+F
(U21a) Cal+Clc+Pl+Qz+Zo = Tr+Scp+F
(U21b) Cal+Clc+Pl+Qz = Scp+Tr+Zo+F
(U21c) Cal+Clc+Qz+Scp+Zo = Pl+Tr+F
(U21d) Cal+Clc+Qz+Scp = Pl+Tr+Zo+F
(U21e) Cal+Clc+Pl+Qz = Scp+Tr+Zo+F
(U22a) Als+Qz+Scp+Tr+Zo = Clc+Pl+F

(U22b) Als+Clc+Qz+Scp+Zo = Pl+Tr+F
(U22c) Als+Clc+Qz+Scp = Pl+Tr+Zo+F
(U23) Als+Scp+Tr+Zo = Cal+Clc+Pl+F
(U24a) Als+Cal+Clc+Pl+Qz = Scp+Tr+F
(U24b) Als+Cc+Clin+Qz+Scp = Pl+Tr+F
(U25a) Als+Cc+Pl+Qz+Tr = Di+Scp+F
(U25b) Als+Cc+Qz+Scp+Tr = Di+Pl+F

(U26) Cal+Di+Mu+Pl = Kfs+Phl+Scp+Zo+F
(U27) Cal+Phl+Pl+Qz+Zo = Di+Mu+Scp+F
(U28) Cal+Di+Mu+Pl+Qz = Kfs+Phl+Scp+F
(U29a) Di+Mu+Scp = Kfs+Phl+Pl+Qz+Zo+F

(U29b) Di+Mu+Qz+Scp = Kfs+Phl+Pl+Zo+F
(U29c) Di+Mu+Qz+Scp+Zo = Kfs+Phl+Pl+F
(U29d) Mu+Phl+Qz+Scp+Zo = Di+Kfs+Pl+F
(U29e) Kfs+Phl+Qz+Scp+Zo = Di+Mu+Pl+F
(U30a) Cal+Clc+Mu+Pl+Qz+Zo = Phl+Scp+F
(U30b) Cal+Clc+Mu+Pl+Qz = Phl+Scp+Zo+F
(U30c) Cal+Clc+Mu+Qz+Scp+Zo = Phl+Pl+ F
(U30d) Cal+Clc+Mu+Qz+Scp = Phl+Pl+Zo+F
(U32a) Als+Cal+Clc+Mu+Pl+Qz = Phl+Scp+F
(U32b) Als+Cal+Clc+Mu+Qz+Scp = Phl+Pl+F
(U33a) Cal+Phl+Pl+Qz+Zo = Di+Kfs+Scp+F
(U33b) Phl+Qz+Scp+Zo = Cal+Di+Kfs+Pl+F
(U33c) Cal+Phl+Qz+Scp+Zo = Di+Kfs+Pl+F
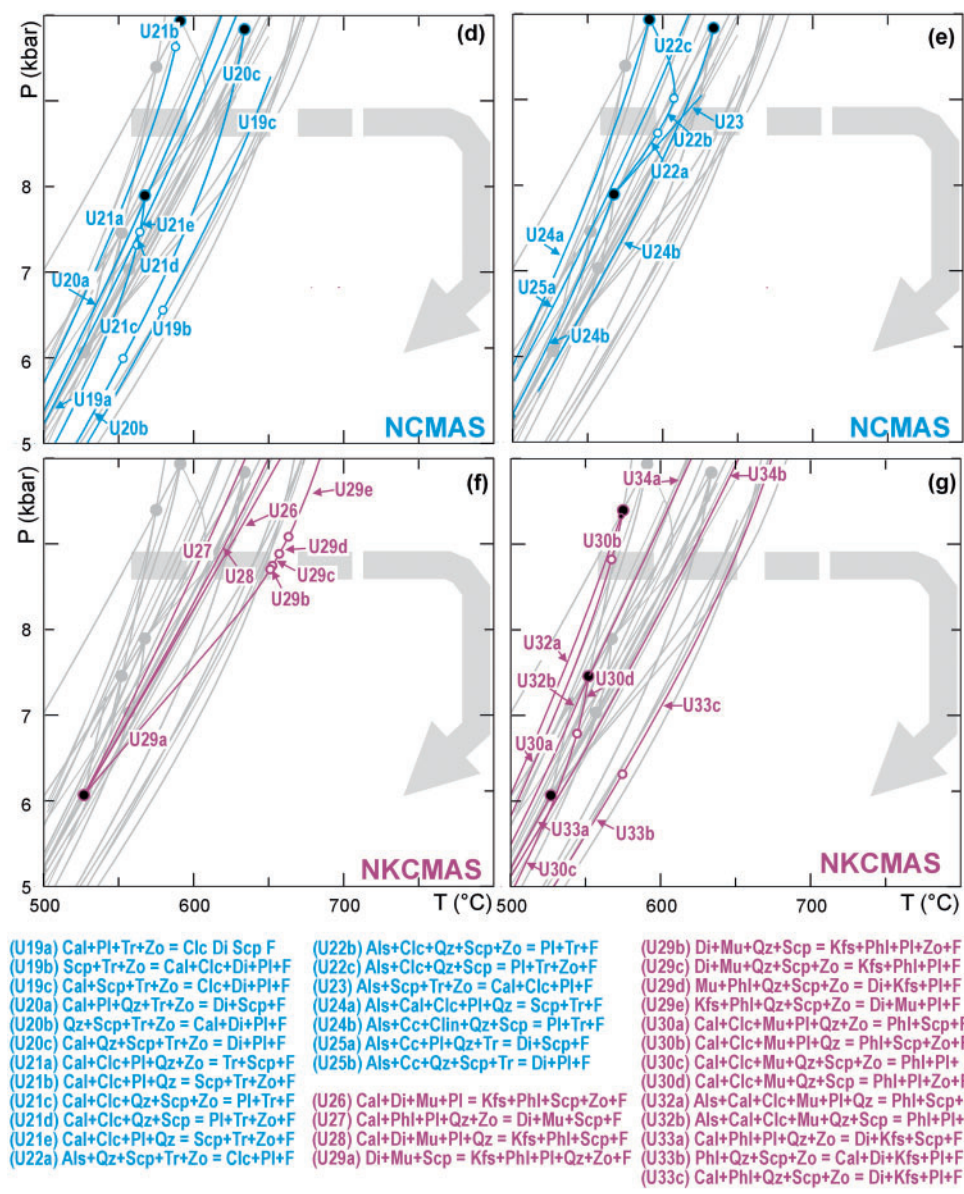
which isobaric univariant and invariant equilibria are effectively 'seen' by the studied samples; (b) isobaric $T–X(CO_2)$ grids allow us to stoichiometrically balance the relevant CO_2-producing univariant equilibria and to recognize the existence of singular points at which a reactant becomes a product or vice versa; (c) mixed-volatile $P–T$ grids (i.e. $P–T$ projections with fluid of variable composition) allow recognition of the crucial role of the isobaric invariant assemblages, in the case of internally buffered systems.

2. It considers Na–Ca solid solutions (plagioclase and scapolite) in the calculation of isobaric $T–X(CO_2)$ grids, thus allowing us to model (a) the isobaric univariant equilibria involving plagioclase and scapolite with compositions that deviate from the end-member composition and (b) the variation in plagioclase and scapolite compositions along these isobaric univariant equilibria.

3. It does not consider any phase in excess, in contrast to the common practice in the calculation of $T–X(CO_2)$ grids [and sometimes also in the calculation of $T–X(CO_2)$ pseudosections; e.g. Kuhn *et al.*, 2005]. This gives the modelled phase diagrams a more general validity, allowing their application also to those calc-silicate rocks in which one or more phases (e.g. calcite, quartz) have been completely consumed during prograde metamorphism.

The very good match between microstructural and compositional observations and the reaction path modelled by our phase diagram approach (see below) strongly supports the reliability of the method. It is worth noting that neither pseudosections nor $T–X(CO_2)$
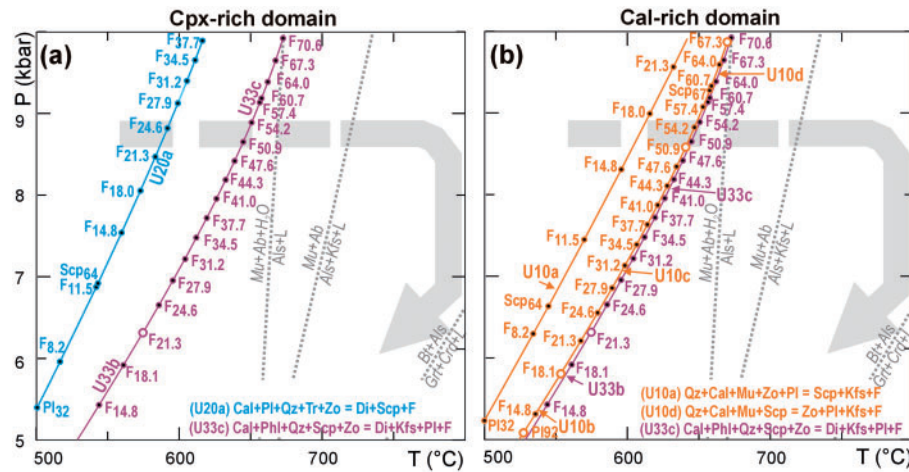
Fig. 10. Same mixed-volatile *P–T* projection as in Fig. 9, showing a selection of the truly univariant curves relevant to Cpx-rich (a) and Cal-rich (b) domains, respectively. Small filled points indicate the variation of fluid, plagioclase and scapolite compositions along each univariant curve. Large filled points are truly invariant points; small open points are singular points. The variations of fluid [$X(CO_2)$], plagioclase (X_{An}) and scapolite (eqAn) compositions along each univariant curve is also shown. The *P–T* evolution inferred from the host anatectic paragneiss (Groppo *et al.*, 2012) is indicated by a grey arrow; muscovite and biotite dehydration melting equilibria are reported as dotted grey lines [modified from Spear *et al.* (1999)].

Table 4: Predicted versus observed mineral assemblages

Isobaric univariant and truly univariant reactions	Observed microstructure	Figure
Cpx-rich domains		
(15) Qz + Tr + Cal → Di (in the Na-rich Pl stability field)	Corroded and lobate inclusions of Qz + Amp + Cal in the core of Cpx porphyroblasts	3c and d
(U20a) Qz + Tr + Cal + Zo + Na-Pl → Di + Scp	Corroded and lobate inclusions of Qz + Amp + Cal + Na-rich Pl ($An_{37–60}$) (but not Scp!) in the core of Cpx porphyroblasts	3c and d
(30) Phl + Cal + Qz → Di + Kfs	Corroded and lobate inclusions of Bt + Cal + Qz in the rim of Cpx porphyroblasts and in Cpx granoblasts; equilibrium relationships between Cpx and Kfs	3c
(U33c) Qz + Phl + Scp + Zo + Cal → Di + Kfs + Ca-Pl	Corroded and lobate inclusions of Qz + Bt + Cal + Scp (eqAn$_{61–67}$) in Cpx granoblasts; sporadic inclusions of Ca-rich Pl (An$_{80–88}$) in the rim of Cpx porphyroblasts (with straight margins against Cpx); equilibrium relationships between Cpx and Kfs	3e and f
(30) Phl + Cal + Qz → Di + Kfs	Corroded and lobate inclusions of Bt + Cal + Qz in Cpx granoblasts; equilibrium relationships between Cpx and Kfs	3e and f
Cal-rich domains		
(5) Mu + Qz + Cal → Zo + Kfs (in the Na-rich Pl stability field)	Corroded and lobate inclusions of Mu + Qz + Cal within Zo; equilibrium relationships between Zo and Kfs; Na-rich Pl (An$_{2–30}$) partially included in Zo (with crystal faces against Zo)	4g and l
(5) Mu + Qz + Cal → Zo + Kfs (in the Scp stability field)	Corroded and lobate inclusions of Mu + Qz + Cal Within Zo; equilibrium relationships between Zo and Kfs	4g and l
(U10d) Qz + Cal + Mu + Scp → Zo + Kfs + Ca-Pl	Corroded and lobate inclusions of Qz + Cal + Mu + Scp (eqAn$_{66–67}$) in Zo; equilibrium relationships between Zo and Kfs	4g, i and l
(U33c) Qz + Phl + Scp + Zo + Cal → D + Kfs + Ca-Pl	Corroded and lobate inclusions of Qz + Bt + Cal + Scp (eqAn$_{61–67}$) in Cpx granoblasts	4a–c

grids alone can provide all the information (i.e. which are the univariant equilibria relevant for the studied samples, and the stoichiometric balancing of the CO_2-producing reactions) that are fundamental for a quantitative, rather than qualitative, study of CO_2-production from calc-silicate rocks.

P–T–X(CO$_2$) evolution

Cpx-rich domains

The key microstructures involving clinopyroxene and K-feldspar in the Cpx-rich domains can be interpreted using the phase diagrams discussed above (Fig. 8a, b and Table 4). The comparison between predicted and
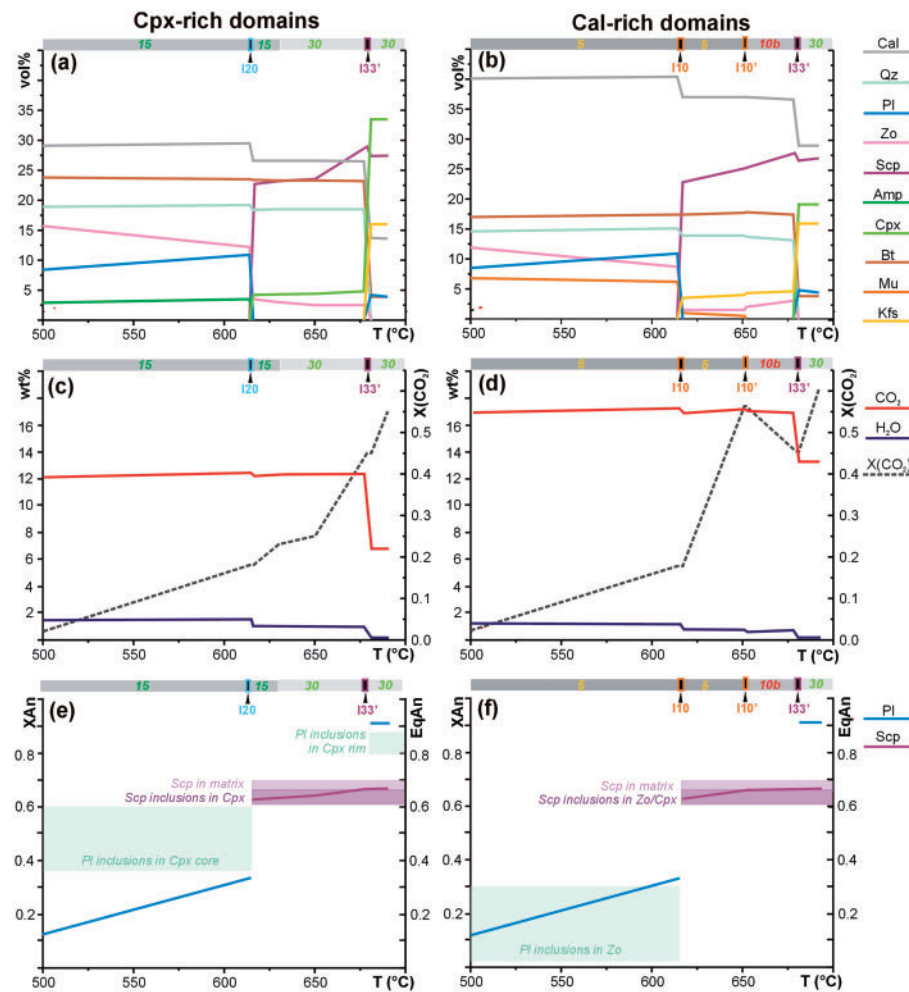
measured compositions of both plagioclase and scapolite is reported in Fig. 11e (see also Supplementary Data Fig. SM3).

1. Microstructural evidence suggests that the cores of the clinopyroxene porphyroblasts grew at the expense of calcite, amphibole, Na-rich plagioclase (An$_{37-60}$) and quartz (Fig. 3c and d). This microstructure can be partially explained by the isobaric univariant reaction 15 (Cal + Qz + Tr → Di) occurring at *T* lower than the isobaric invariant point I20 (i.e. in the Na-rich Pl stability field; Fig. 8a). However, such a reaction should result in the 'passive' inclusion of Na-rich Pl within Cpx cores, whereas in most cases Na-rich Pl included in Cpx cores shows corroded and lobate margins (Fig. 3d), suggesting its 'active' participation as a reactant in the Cpx-forming reaction. Na-rich plagioclase is a reactant in the Cpx-forming truly univariant reaction U20a (Fig. 10a), corresponding to the isobaric invariant point I20 (Fig. 8b), thus suggesting that the system evolved along the isobaric univariant equilibrium 15 (i.e. it remained internally buffered) until it reached the point I20.

2. The rims of clinopyroxene porphyroblasts contain small corroded inclusions of quartz, calcite and biotite (Fig. 3c) and are in equilibrium with K-feldspar (large K-feldspar inclusions with straight margins against clinopyroxene; Fig. 3c). This microstructure is compatible with its growth through the isobaric univariant reaction 30 (Cal + Phl + Qz → Di + Kfs), suggesting that reaction 15 (and its buffering ability) ceased owing to the complete consumption of a reactant (e.g. amphibole). Moreover, the sporadic inclusions of Ca-rich plagioclase (An$_{80-88}$) (with straight margins against Cpx) observed in the rims of clinopyroxene porphyroblasts suggest the attainment of the isobaric invariant point I33' (Fig. 8b) (univariant reaction U33c: Cal + Phl + Qz + Scp + Zo → Di + Kfs + Ca-Pl + F; Fig. 10a).

3. The isobaric univariant reaction 30 could be also responsible, at least partially, for the growth of clinopyroxene granoblasts at the expense of biotite,

Fig. 11. Modal (vol. %) evolution (a, b), amounts (wt %) and composition of the produced fluids (c, d), and modeled vs measured compositions of plagioclase (X_{An}) and scapolite (EqAn) (e, f) for the Cpx-rich (a, c, e) and Cal-rich (b, d, f) domains along the inferred *T*–*X*(CO$_2$) paths reported in Fig. 8a and c, respectively. The isobaric univariant curves and invariant points followed by the *T*–*X*(CO$_2$) paths are reported on the top of each diagram (same colors as in Fig. 8b and d).

calcite and quartz (Fig. 3e and f). However, this reaction alone is not able to explain the 'active' role of scapolite as a reactant phase in the Cpx-forming reaction, which is suggested by its corroded and lobate margins against the host clinopyroxene (Fig. 3f). Scapolite is a reactant in the Cpx- and Kfs-forming univariant reaction U33c (Cal + Phl + Qz + Scp + Zo → Di + Kfs + Pl + F) (Fig. 10a), corresponding to the isobaric invariant point I33' (Fig. 8b); this reaction predicts the formation of clinopyroxene in equilibrium with K-feldspar and Ca-rich plagioclase, at the expense of scapolite, biotite, zoisite, calcite and quartz, and it is therefore fully compatible with the observed microstructures illustrated in Fig. 3e and f. It is worth mentioning that the truly univariant reaction U33c is modelled at $P > 6.2$ kbar, being limited toward lower P by a singular point (see Figs 9g and 10a).

4. When one of the reactants of reaction U33c (i.e. zoisite) was completely exhausted, the system further evolved along isobaric univariant reaction 30. The lack of garnet, predicted to appear for $X(CO_2) > 0.7$ (Fig. 8b), suggests that reaction 30 (and its buffering ability) ceased owing to the complete consumption of quartz (which is indeed very scarce). During further heating to peak T conditions the system crossed the fluid-absent reaction Pl + Cal → Scp, entering the Cal + Cpx + Kfs + Scp + Bt stability field (Fig. 8a).

5. The inferred $P–T–X(CO_2)$ evolution (Fig. 8a) points to a final peak mineral assemblage characterized by the absence of plagioclase (i.e. Cpx + Kfs + Cal + Scp + Bt + Ttn), which is apparently in contrast to the observed mineral assemblage. However, most of the peak scapolite was probably replaced by symplectitic aggregates of plagioclase + calcite during retrogression; these microstructures have been widely described (e.g. Harley & Buick, 1992; Fitzsimons & Harley, 1994; Bhowmik *et al.*, 1995; Stephenson & Cook, 1997; Mathavan & Fernando, 2001) and interpreted as the breakdown products of scapolite during cooling (i.e. fluid-absent reaction: Scp → Pl + Cal).

Cal-rich domains

The key microstructures involving zoisite, clinopyroxene and K-feldspar in the Cal-rich domains can be also interpreted using the phase diagrams discussed above (Fig. 8c, d and Table 4). The comparison between predicted and measured compositions of both plagioclase and scapolite is reported in Fig. 11f (see also Supplementary Data Fig. SM3).

1. Microstructural evidence suggests that zoisite grew at the expense of quartz, calcite, muscovite and scapolite; all these phases occur as very fine-grained and corroded inclusions within zoisite (Fig. 4g, i, l). Microstructures are ambiguous concerning Na-rich plagioclase, which is partially included in zoisite; Na-rich plagioclase (An_{2-30}) is coarser grained than the

other inclusions, and locally shows crystal faces against zoisite (Fig. 4g, l), thus suggesting that it was locally in equilibrium with it. K-feldspar is also included in zoisite, and occurs as relatively coarse-grained inclusions with crystal faces against zoisite (Fig. 4g, l), thus suggesting equilibrium relationships between them. Overall, the zoisite-bearing microstructural sites can be described in the NKCAS-HC subsystem and, involving seven mineral phases (zoisite, calcite, quartz, plagioclase, scapolite, muscovite and K-feldspar), define an isobaric invariant assemblage. More specifically, this assemblage corresponds to that of the isobaric invariant point I10' (Fig. 8d). The corresponding truly univariant reaction in the mixed-volatile $P–T$ projection at 9 kbar (Fig. 10b), is the Zo- and Kfs-forming reaction U10d (Qz + Cal + Mu + Scp → Zo + Ca-rich Pl + Kfs + F). This reaction is fully compatible with most of the observed microstructures (i.e. the fine-grained inclusions within zoisite and the equilibrium relationships between zoisite and K-feldspar). It is worth mentioning that the truly univariant reaction U10d is modelled in a relatively narrow P range ($8.6 < P < 9.9$ kbar), being limited toward both lower and higher P by two singular points (see Fig. 9c and 10b). The Na-rich plagioclase inclusions within zoisite may be justified by the system reaching the isobaric invariant point I10' from T compatible with the stability of Na-rich plagioclase (i.e. through the isobaric invariant point I10 / truly univariant curve U10a, at $T < 620°C$) (Fig. 8c).

2. The Cpx- and Kfs- forming univariant reaction U33c (Cal + Phl + Qz + Scp + Zo → Di + Kfs + Pl + F) (Fig. 10b) is responsible for the growth of clinopyroxene granoblasts at the expense of quartz, calcite, biotite and scapolite, as suggested by microstructural evidence (Fig. 4a-c).

3. Once zoisite was completely exhausted, the system probably evolved along the isobaric-univariant reaction 30 (Fig. 8c); as discussed for the Cpx-rich domains, reaction 30 probably ceased when quartz was completely consumed. Further heating to peak T conditions resulted in the disappearance of plagioclase according to the fluid-absent reaction Pl + Cal → Scp (i.e. the peak assemblage: Cpx + Kfs + Cal + Scp + Bt + Ttn).

4. Symplectitic aggregates of plagioclase + calcite formed at the expense of scapolite are interpreted as in the Cpx-rich domains; that is, as the breakdown products of scapolite during cooling.

Fluid behaviour: buffering in a completely closed system or buffering accompanied by infiltration?

The observed microstructures combined with the results of phase diagram modeling strongly suggest that the equilibrium mineral assemblages in the studied calc-silicate rock buffered the composition of the pore fluid during prograde metamorphism (Fig. 8a and c).

J_ID: **PETROLOGY** Customer A_ID: **EGX005** Copyedited by: **PR** Manuscript Category: **Original Article** Cadmus Art: **O**

NOT FOR PUBLIC RELEASE

Most of the observed microstructures, in fact, reflect either isobaric univariant assemblages or isobaric invariant assemblages (i.e. truly univariant assemblages in the corresponding mixed-volatile *P–T* projection); for completely open-system behavior, isobaric divariant assemblages would have been observed instead (e.g. Trommsdorff, 1972; Hewitt, 1973; Kerrick, 1974; Rice & Ferry, 1982). However, mineral reactions may control fluid composition even in cases of fluid infiltration (e.g. Greenwood, 1975; Rice & Ferry, 1982; Ferry, 1983a; Ague & Rye, 1999); that is, intermediate conditions between complete internal buffering behavior and complete external buffering behavior. The observed versus predicted modal amounts of minerals can provide a key to understanding whether buffering occurred in a completely closed system or was accompanied by infiltration (e.g. Greenwood, 1975; Rice & Ferry, 1982; Ferry, 1983a) and, in the second case, to quantitatively estimate the amount and composition of external fluid that interacted with the rock during metamorphism. This method is applied to discuss the fluid behavior in the studied calc-silicate rock and to quantitatively estimate the compositions and volumes of the fluid produced.

Cpx-rich domains

In the Cpx-rich domains the composition of the fluid is controlled by the mineral assemblages corresponding to the isobaric univariant curves 15 and 30 and to the isobaric invariant points I20 and I33' (Fig. 8a and b). The amounts of clinopyroxene and K-feldspar produced in a completely internally buffered system along the isobaric univariant curves 15 and 30 are significantly lower than the observed mineral modes. This happens because along the isobaric univariant reaction curves, changes in the mode of minerals are very gradual (Fig. 11a).

In an internally buffered system, however, sudden and volumetrically significant appearances of new phases and the simultaneous disappearance of previously abundant phases occur at the isobaric invariant points (Greenwood, 1975; Rice & Ferry, 1982). In our case, at the isobaric invariant point I20, diopside is produced through reaction U20a (Cal + Pl + Qz + Tr + Zo → Di + Scp + F), whereas at the isobaric invariant point I33', diopside and K-feldspar are produced through reaction U33c (Cal + Phl + Qz + Scp + Zo → Di + Kfs + Pl + F) (Fig. 10a). Figure 11a shows the changes in mineral abundances along the inferred $T–X$(CO$_2$) evolution, as predicted by the pseudosection of Fig. 8a (see also Fig. 12 and Supplementary Data Fig. SM4); it is evident that abrupt changes in the mineral modes occur at the two invariant points I20 and I33', whereas along the isobaric univariant curves only slight modal changes occur. According to Fig. 11a, 4·2 vol. % of clinopyroxene is produced at I20, and 28·7 vol. % of clinopyroxene and 16·0 vol. % of K-feldspar are produced at I33'. Combining the amounts of clinopyroxene and K-feldspar produced along the univariant reactions 15 and 30 and those produced at the invariant points I20 and I33',

a total production of 33·6 vol. % of Cpx and 16·0 vol. % of Kfs is predicted for a completely internally buffered system. The close similarity between the modal amounts of minerals observed in the Cpx domains (i.e. Cpx: 39 vol. %; Kfs: 14 vol. %) and those predicted by the pseudosection (i.e. Cpx: 34 vol. %; Kfs: 16 vol. %) (Fig. 11a, Tables 5 and 6 and Supplementary Data Fig. SM4), suggests that little or no externally derived fluid interacted with the rock.
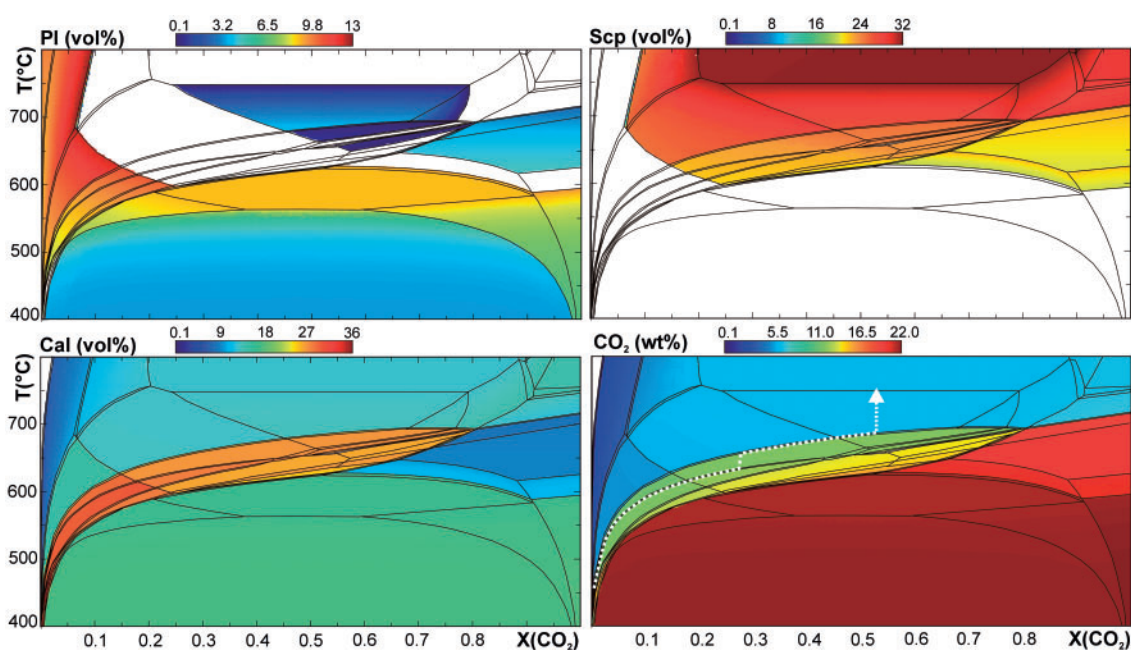
Cal-rich domains

In the Cal-rich domains the composition of the fluid is controlled by the mineral assemblages corresponding to the isobaric univariant curves 5, 10 b and 30 and to the isobaric invariant points I10, I10' and I33' (Fig. 8c and d). Similarly to the case for the Cpx-rich domains, the predicted modes of K-feldspar and clinopyroxene produced along the isobaric univariant curves 5 and 30 are significantly lower than the observed modes, whereas most of the K-feldspar and clinopyroxene is produced at isobaric invariant points. More specifically, at the isobaric invariant point I10, K-feldspar (and scapolite) are produced through reaction U10a (Qz + Cal + Mu + Zo + Pl → Scp + Kfs + F), at the isobaric invariant point I10', K-feldspar and zoisite are produced through reaction U10d (Qz + Cal + Mu + Scp → Zo + Pl + Kfs + F) and at the isobaric invariant point I33', K-feldspar and clinopyroxene are produced through reaction U33c (Cal + Phl + Qz + Scp + Zo → Di + Kfs + Pl + F) (Fig. 10b).

The modal evolution of the Cal-rich domains along the inferred $T–X$(CO$_2$) evolution is shown in Fig. 11b (see also Fig. 13 and Fig. SM5). Abrupt changes in the mineral modes occur at the two invariant points I10 and I33' (and to a lesser extent also at I10'), whereas along the isobaric univariant curves only slight modal changes occur. According to the pseudosection results, 4·3 vol. % of K-feldspar is produced at I10, 0·3 vol. % of K-feldspar and 0·5 vol. % of zoisite are produced at I10', and 11·3 vol. % of K-feldspar and 19·1 vol. % of clinopyroxene are produced at I33'. Combining the amounts of K-feldspar and clinopyroxene produced along the univariant reactions 5 and 30 and those produced at the invariant points I10, I10' and I33', a total of 15·9 vol. % of Kfs and 19·2 vol. % of Cpx are predicted for a completely internally buffered system. The close similarity between the modal amounts of minerals observed in the Cal domains (i.e. Kfs: 17 vol. %; Cpx: 22 vol. %) and those predicted by the pseudosection (i.e. Kfs: 16 vol. %; Cpx: 19 vol. %) (Fig. 11b, Tables 5 and 6 and Supplementary Data Fig. SM5) suggests that little or no externally derived fluid interacted with the rock.

Amounts and compositions of fluids released by prograde devolatilization reactions

The results obtained from the phase diagram modeling indicate that both the Cpx- and Cal- rich domains behaved as nearly closed systems during prograde metamorphism.

Fig. 12. Predicted plagioclase, scapolite and calcite modes (vol. %) and CO_2 amounts (wt %) for the Cpx-rich domains, based on the $T–X(CO_2)$ pseudosection of Fig. 8a. Colours from blue to red imply higher proportions as shown in each legend. The complete set of modes for all the mineral phases is reported in Supplementary Data Fig. SM4.

Table 5: Predicted versus observed mineral amounts (vol. %)

	Bt	Cal	Cpx	Kfs	Pl*	Qz	Scp	Ttn	Zo
Cpx-rich domains									
Predicted at 760°C, 9 kbar, $X(CO_2) = 0.6$	3·9	13·2	33·6	16·0			32·1	1·3	
Observed	4	15	39	14	18	1	8	1	
Cal-rich domains									
Predicted at 760°C, 9 kbar, $X(CO_2) = 0.6$	3·7	28·3	19·2	15·9			31·6	1·2	
Observed	1	29	22	17	19	<1	9	1	2

*Most of the plagioclase in both Cpx- and Cal-rich domains derives from scapolite breakdown during retrogression (fluid-absent reaction: Scp → Pl + Cal).

Table 6: Calculated amounts of fluid released by Cpx-rich domains

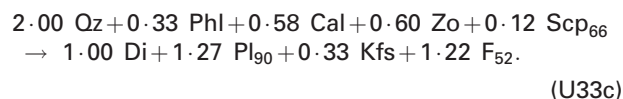| Reaction U20a (8·8 kbar, 590°C)					Reaction U33c (8·8 kbar, 650°C)				
	Molar V ($cm^3 mol^{-1}$)	Stoich. coeff.	No. of mol	V (cm^3)		Molar V ($cm^3 mol^{-1}$)	Stoich. coeff.	No. of mol	V (cm^3)
Reactants									
Qz	22·92	0·40	0·25	5·8	Qz	23·00	2·00	8·94	205·7
Tr	274	0·20	0·13	34·4	Phl	150·02	0·33	1·48	221·3
Cal	37·1	1·13	0·71	26·3	Cal	37·17	0·58	2·59	96·4
Zo	137·52	0·83	0·52	71·7	Zo	137·87	0·60	2·68	369·8
Pl_{34}	100·68	1·61	1·01	101·8	Scp_{66}	340·01	0·12	0·54	182·4
Products									
					Cpx	67·03	1·00	4·47	299·7
Scp_{63}	339·62	0·95	0·60	202·6	Pl_{90}	100·77	1·27	5·68	572·2
Cpx*	66·89	1·00	0·63	42·0	Kfs*	108·45	0·33	1·48	160·0
F_{23}	23·01	0·80	0·50	11·6	F_{52}	28·47	1·22	5·45	155·3
	V (cm^3)	No. of mol	Wt (g)	Wt %		V (cm^3)	No. of mol	Wt (g)	Wt %
rock	1000		2700·0		rock	1000		2700·0	
CO_2		0·12	5·1	0·2	CO_2		2·84	125·1	4·6%

*The phase whose modal amount has been used to calculate the amount of released fluid.
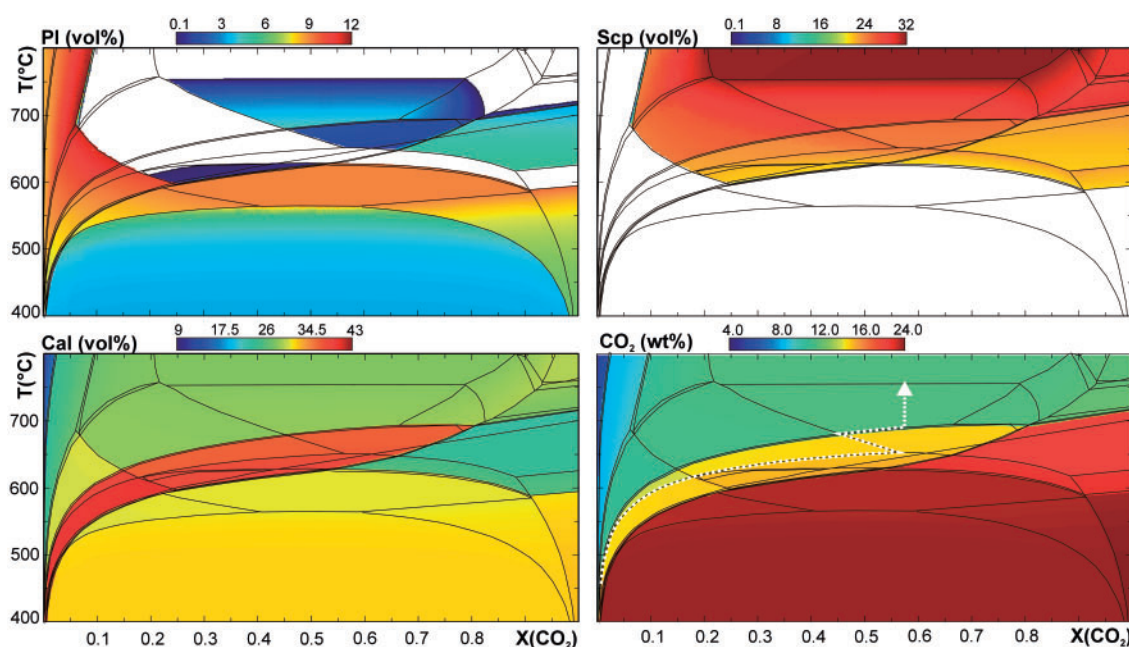
Fig. 13. Predicted plagioclase, scapolite and calcite modes (vol. %) and CO_2 amounts (wt %) for the Cal-rich domains, based on the $T–X(CO_2)$ pseudosection of Fig. 8c. Colours from blue to red imply higher proportions as shown in each legend. The complete set of modes for all the mineral phases is reported in Supplementary Data Fig. SM5.

Other studies have already pointed out the possibility that marly layers might not have been infiltrated by large volumes of reactive fluids during prograde metamorphism, even if intercalated with rocks characterized by a significant fluid infiltration (e.g. Cartwright & Buick, 1995; Nabelek, 2002). In such a nearly closed system, the fluid was mostly produced at the isobaric invariant points I20 and I33′ (Cpx-rich domains) and I10, I10′ and I33′ (Cal-rich domains) (Fig. 8), where abrupt changes in mineral modes also occurred (Fig. 11a and b). The amount of fluid produced at each isobaric invariant point can be directly extrapolated, to a first approximation, from the $T–X(CO_2)$ pseudosections (Figs 11c, d, 12 and 13). Figure 11c and d shows that in both the Cpx- and Cal-rich domains most of the CO_2 is produced at the isobaric invariant point I33′ (i.e. truly univariant reaction U33c), whereas minor amounts of CO_2 are produced at the other isobaric invariant points. More specifically, in the Cpx-rich domain < 0.1 and $\sim$5 wt % of CO_2 are produced at I20′ and I33′, respectively; in the Cal-rich domain <0.3, <0.1 and $\sim$3.5 wt % of CO_2 are produced at I10, I10′ and I33′, respectively.

A different and complementary approach to constrain the amounts of CO_2 released per volume unit of reacting rock is that of using the balanced truly univariant reactions U20a, U10a, U10d and U33c modelled in the mixed-volatile *P–T* projection of Figs 9 and 10. Let us consider the truly univariant reaction U33c, stoichiometrically balanced at a pressure of 8.8 kbar:

$$2.00 \ Qz + 0.33 \ Phl + 0.58 \ Cal + 0.60 \ Zo + 0.12 \ Scp_{66}$$
$$\rightarrow \ 1.00 \ Di + 1.27 \ Pl_{90} + 0.33 \ Kfs + 1.22 \ F_{52}.$$

(U33c)

As shown in Figs 8 and 11a, b, this reaction represents the only Kfs-forming reaction 'seen' by the Cpx-rich domains; the same reaction is the only Cpx-forming reaction 'seen' by the Cal-rich domains. This means that the modal amounts of K-feldspar and clinopyroxene, modelled (and observed) in the Cpx- and Cal-rich domains respectively, can be considered as monitors of the volume of fluid released through reaction U33c at *c.* 650°C, 8.8 kbar. In the Cpx-rich domains, 16 vol. % of K-feldspar is predicted (and 14 vol. % is observed), corresponding to 160 cm^3 of K-feldspar per 1000 cm^3 of rock. This volume amount corresponds to 1.48 moles of K-feldspar and, given the stoichiometry of the reaction, the number of moles of the fluid produced by this reaction (F_{52}) is 5.45, and the number of moles of CO_2 is 2.84 (Table 6). Considering that 1 mole of CO_2 weighs 44 g, the total amount of CO_2 released by the truly univariant reaction U33c per 1000 cm^3 of rock is 125 g, corresponding to 4.6 wt % of CO_2. In terms of volumes, the molar volume of a fluid with $X(CO_2) = 0.52$ at 650°C, 8.8 kbar is 28.47 cm^3 mol^{-1} [calculated using the equation of state for H_2O–CO_2 fluid of Holland & Powell (1998)]; therefore the volume of fluid produced is 155 cm^3 per 1000 cm^3 of reacting rock (i.e. 15.5 vol. % of fluid) (Table 6).
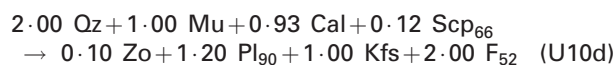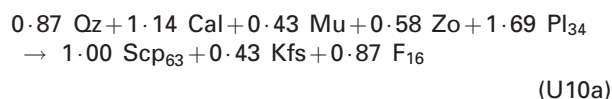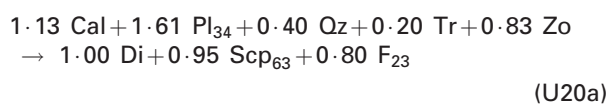
Similarly, the modelled modal amount of clinopyroxene (19.1 vol. %; compared with 20 vol. % observed) in the Cal-rich domains gives an amount of produced CO_2 of 79.7 g (1.81 mol) per 1000 cm^3 of rock (corresponding to 3.0 wt % of CO_2). In terms of volumes, 99 cm^3 of fluid with $X(CO_2) = 0.52$ are produced per 1000 cm^3 of reacting rock (i.e. 9.9 vol. % of fluid) by the truly univariant reaction U33c (Table 7).

Table 7: Calculated amounts of fluid released by Cal-rich domains

	Reaction U10a (8·8 kbar, 600°C)				Reaction U10d (8·8 kbar, 650°C)				Reaction U33c (8·8 kbar, 650°C)			
	Molar V (cm³ mol⁻¹)	Stoich. coeff.	No. of mol	V (cm³)	Molar V (cm³ mol⁻¹)	Stoich. coeff.	No. of mol	V (cm³)	Molar V (cm³ mol⁻¹)	Stoich. coeff.	No. of mol	V (cm³)
Reactants												
Qz	22·93	0·87	0·80	18·4	23·00	2·00	0·07	1·7	23·00	2	5·70	131·1
Mu	140·9	0·43	0·40	55·9	37·17	0·93	0·03	1·3	150·02	0·33	0·94	141·1
Cal	37·11	1·14	1·05	39·0	14·12	1·00	0·04	0·5	37·17	0·58	1·65	61·4
Zo	137·58	0·58	0·54	73·6	340·01	0·12	0·00	1·5	137·87	0·6	1·71	235·7
Pl₃₄	100·69	1·69	1·56	157·1					340·01	0·12	0·34	116·3
(Qz/Cal/Mu/Scp₆₆)												
					137·87	0·1	0·04	5·0	67·03	1·00	2·85	191·0
Kfs*	108·35	0·43	0·40	43·0	100·77	1·2	0·44	43·9	100·77	1·27	3·62	364·7
Scp₆₃	339·69	1·00	0·92	313·5	108·45	1·0	0·36	39·3	108·45	0·33	0·94	102·0
F₁₆	21·87	0·87	0·80	17·6	28·47	2·0	0·73	20·6	28·47	1·22	3·48	99·0

	V (cm³)	No. of mol	Wt (g)	Wt %		V (cm³)	No. of mol	Wt (g)	Wt %		V (cm³)	No. of mol	Wt (g)	Wt %
rock	1000		2700·0		rock	1000		2700·0		rock	1000		2700·0	
CO₂		0·13	5·7	0·2	CO₂		0·38	16·6	0·6	CO₂		1·81	79·7	3·0

*The phase whose modal amount has been used to calculate the amount of released fluid.

The same approach, applied to the other truly univariant reactions U20a, U10a and U10d, stoichiometrically balanced at the pressure of 8·8 kbar:

$$1·13\ Cal + 1·61\ Pl_{34} + 0·40\ Qz + 0·20\ Tr + 0·83\ Zo \rightarrow\ 1·00\ Di + 0·95\ Scp_{63} + 0·80\ F_{23}$$

(U20a)

$$0·87\ Qz + 1·14\ Cal + 0·43\ Mu + 0·58\ Zo + 1·69\ Pl_{34} \rightarrow\ 1·00\ Scp_{63} + 0·43\ Kfs + 0·87\ F_{16}$$

(U10a)

$$2·00\ Qz + 1·00\ Mu + 0·93\ Cal + 0·12\ Scp_{66} \rightarrow\ 0·10\ Zo + 1·20\ Pl_{90} + 1·00\ Kfs + 2·00\ F_{52}$$

(U10d)

respectively gives 5·1 g (0·12 mol; reaction U20a), 5·7 g (0·13 mol; reaction U10a) and 16·6 g (0·38 mol; reaction U10d) of CO_2 produced per 1000 cm³ of reacting rock, corresponding to 0·2 wt %, 0·2 wt % and 0·6 wt %, respectively (Tables 6 and 7).

From the calculations presented above it follows that, on average, 110 g (2·5 mol) of CO_2 per 1000 cm³ of reacting rock have been produced during prograde metamorphism of this type of scapolite-bearing calc-silicate rock. The Cpx-rich domains produced more CO_2 than the Cal-rich domains, thus suggesting that carbonate-poor marly sediments could be more efficient CO_2 sources than carbonate-rich sediments. Overall, these are indeed significant amounts of CO_2, especially considering that the decarbonation reactions have not been driven by infiltration of reactive fluids.

To quantify the amount of CO_2 produced at the orogen scale, a precise estimate of the volume of these calc-silicate rocks in the whole Himalayan belt is required. However, calc-silicate rocks have often been neglected in previous geological studies, and in most of the Himalayan geological maps they have not been differentiated from the host metapelites. Based on our field data we roughly estimate that this specific calc-silicate type could represent ∼1–3 vol. % of the whole GHS metasedimentary sequence (e.g. Rolfo et al., 2015, 2017). Kerrick & Caldeira (1999) suggested that the entire volume of GHS rocks that underwent Himalayan metamorphism was ∼9 × 10⁶ km³ (considering that the exposed GHS outcrop area is ∼2·5 × 10⁵ km² and that ∼35 km of overburden was removed by erosion). According to these rough estimates, the volume of the scapolite-bearing calc-silicate rocks studied here is therefore ∼(0·9–2·7) × 10⁵ km³. This would result in a total metamorphic CO_2 production of ∼(2–7) × 10¹⁷ mol, or (1–3) × 10¹⁰ Mt, of CO_2. Considering that prograde metamorphism in the Himalayas lasted ∼20 Myr (e.g. Kohn, 2014; see also Kerrick & Caldeira, 1999), and assuming that all the CO_2 produced in that period was expelled to the surface with a constant flux rate, the calculated metamorphic CO_2 flux would be (1·1–3·4) × 10¹⁰ mol a⁻¹, corresponding to an annual mass flux of (0·5–1·5) × 10³ Mt a⁻¹. These values are one order of magnitude lower than the present-day CO_2 fluxes estimated by Becker et al. (2008) (4·0 × 10⁴ Mt a⁻¹) and Evans et al. (2008) (0·9 × 10⁴ Mt a⁻¹) based on the CO_2 degassed from spring waters, but only slightly lower than the past metamorphic CO_2 fluxes estimated by Kerrick & Caldeira (1999) (∼10¹¹ mol a⁻¹; 4·4 × 10³ Mt a⁻¹). However, our data should be considered as minimum values because (1) they refer to only one calc-silicate type among more than 10 CO_2-source rock types recognized so far in the GHS (Rolfo et al., 2017) and (2) recent studies on metamorphic fluid flow have shown that the release of metamorphic CO_2 to the atmosphere occurs in pulses (e.g. Skelton, 2013) that are shorter lived in comparison with the assumed duration of prograde metamorphism.

CONCLUSIONS

The results of this study demonstrate that phase petrology modeling combined with detailed microstructural studies is a powerful method to investigate the nature of metamorphic CO_2-producing reactions and to quantify the amount of CO_2 released during prograde metamorphism of scapolite-bearing metacarbonate rocks. This approach is an alternative to the 'reaction progress' method, which is mostly applied to relatively open systems (i.e. where decarbonation reactions were driven by reactive fluid infiltration), and is particularly suitable to investigate internally buffered, nearly closed systems.

Overall, the results of this study can be summarized as follows.

Importance of considering Na–Ca solid solutions. The use of simplified model systems (six or fewer components), the overlooking of solid solutions such as those of plagioclase and scapolite, and the assumption that the system is calcite and quartz oversaturated have often led to an oversimplified interpretation of the CO_2-producing reactions in scapolite-bearing calc-silicate rocks. Our study allowed identification of scapolite-bearing, CO_2-producing, equilibria that have never been investigated before, and that could not be detected without considering Na–Ca solid solutions in the calculation (compare Figs 6 and 7 with Supplementary Data Figs SM1 and 2).

Role of isobaric invariant (i.e. truly univariant) equilibria. Our results suggest that the investigated calc-silicate rocks behaved as a nearly closed system during prograde metamorphism, and that most of the observed key microstructures correspond to isobaric invariant assemblages. The importance of isobaric invariant equilibria has been acknowledged since the pioneering work of Kerrick (1974) and Greenwood (1975). What is underlined here is that, because in such nearly closed systems the fluid is mostly produced at the isobaric invariant points, a precise knowledge of what happens at the isobaric invariant points is crucial for quantitatively estimating the amount and composition of the produced fluid.

Characterization of isobaric invariant (truly univariant) equilibria. Given that pressure conditions are independently known, $T–X(CO_2)$ pseudosections are an invaluable tool to model the $T–X(CO_2)$ evolution of calc-silicate rocks; pseudosections, in fact, are modeled for specific (and thus realistic) bulk-rock compositions and allow consideration of the effects of Mg–Fe substitution in mafic minerals, which are generally approximated by reduced activities in the conventional $T–X(CO_2)$ grids. However, pseudosections alone do not allow us to understand what happens at the isobaric invariant points. It is only through mixed-volatile $P–T$ projections that the isobaric invariant (truly univariant) equilibria can be fully characterized. This approach allows us to identify which are the reactants and products of the isobaric invariant reactions (which can change along the same equilibrium curve owing to the presence of singular points) and to estimate their compositions; moreover, we can stoichiometrically balance the reactions that occur at isobaric invariant points and are crucial for estimating the amounts of fluid released.

Amounts of produced fluid. Our study demonstrates that scapolite-bearing calc-silicate rocks may act as a CO_2 source during prograde heating, releasing internally derived CO_2-rich fluids through clinopyroxene-, K-feldspar- and zoisite-forming, and scapolite-consuming, reactions. We have demonstrated that, on average, 2·5 mol of CO_2 per 1000 cm^3 of reacting rock have been produced during prograde metamorphism of this type of scapolite-bearing calc-silicate rock. These are significant amounts of CO_2, especially considering that decarbonation reactions have not been driven by infiltration of reactive fluids. Scapolite-bearing calc-silicate rocks similar to that studied here are abundant in the Himalayan orogen, where they often form layers hundreds of meters thick within anatectic metapelites (Rolfo *et al.*, 2015, 2017). A preliminary and first-order extrapolation of these values to the whole Himalayan belt would suggest a total metamorphic CO_2 production of $\sim(2–7) \times 10^{17}$ mol, corresponding to an annual mass flux of $(0·5–1·5) \times 10^3$ Mt a^{-1}. The fate of this CO_2-rich fluid is nevertheless uncertain and further studies need to be undertaken to understand if such CO_2-rich fluids are able to reach the Earth's surface, or if CO_2 was sequestered through graphite and/or carbonate precipitation during cooling (e.g. Groppo *et al.*, 2013*b*; Craw & Upton, 2014).

REFERENCES

Abart, R., Connolly, J. A. D. & Trommsdorff, V. (1992). Singular point analysis: construction of Schreinemakers projections for systems with a binary solution. *American Journal of Science* **292**, 778–805.

Ague, J. J. (2000). Release of CO_2 from carbonate rocks during regional metamorphism of lithologically heterogeneous crust. *Geology* **28**, 1123–1126.

Ague, J. J. (2002). Gradients in fluid composition across meta-carbonate layers of the Wepawaug Schist, Connecticut, USA. *Contributions to Mineralogy and Petrology* **143**, 38–55.

Ague, J. J. (2003). Fluid infiltration and transport of major, minor, and trace elements during regional metamorphism of carbonate rocks, Wepawaug schist, Connecticut, USA. *American Journal of Science* **303**, 753–816.

Ague, J. J. & Rye, D. M. (1999). Simple models of CO_2 release from metacarbonates with implications for interpretation of directions and magnitudes of fluid flow in the deep crust. *Journal of Petrology* **40**, 1443–1462.

Baker, J., Holland, T. J. B. & Powell, R. (1991). Isograds in intern-ally buffered systems without solid solutions: principles and examples. *Contributions to Mineralogy and Petrology* **106**, 170–182.

Becker, J. A., Bickle, M. J., Galy, A. & Holland, T. J. B. (2008). Himalayan metamorphic CO_2 fluxes: Quantitative con-straints from hydrothermal springs. *Earth and Planetary Science Letters* **265**, 616–629.

Bhowmik, S. K., Dasgupta, S., Hoernes, S. & Bhattacharya, P. K. (1995). Extremely high-temperature calcareous granulites from the Eastern Ghats, India: evidence for isobaric cooling, fluid buffering, and terminal channelized fluid flow. *European Journal of Mineralogy* **7**, 689–703.

Bordet, P. (1961). *Recherches géologiques dans l'Himalaya du Nepal, région du Makalu*. Centre National de la Recherche Scientifique.

Bucher, K. & Grapes, R. (2011). *Petrogenesis of Metamorphic Rocks*, 8th edn. Springer.

Burchfield, B. C., Chen, Z. L., Hodges, K. V., Liu, Y. P., Royden, L. H., Deng, C.R. & Xu, J. N. (1992). The South Tibetan Detachment System, Himalayan Orogen. In: *Geological Society of America, Special Papers* **269**, 1–41.

Carmichael, D. M. (1991). Univariant mixed-volatile reactions: pressure–temperature phase diagrams and reaction iso-grads. *Canadian Mineralogist* **29**, 741–754.

Carosi, R., Lombardo, B., Molli, G., Musumeci, G. & Pertusati, P. C. (1998). The South Tibetan Detachment System in the Rongbuk valley, Everest region. Deformation features and geological im-plications. *Journal of Asian Earth Sciences* **16**, 299–311.

Cartwright, I. & Buick, I. S. (1995). Formation of wollastonite-bearing marbles during late-regional metamorphic chan-nelled fluid flow in the Upper Calc-silicate Unit, Reynolds Range Group, central Australia. *Journal of Metamorphic Geology* **13**, 397–418.

Cartwright, I., Buick, I. S. & Harley, S. L. (1997). Timing and mechanisms of carbon isotope exchange in granulite-facies calc-silicate boudins, Rauer Group, East Antarctica. *American Mineralogist* **82**, 392–404.

Castelli, D., Rolfo, F., Groppo, C. & Compagnoni, R. (2007). Impure marbles from the UHP Brossasco–Isasca Unit (Dora–Maira Massif, western Alps): evidence for Alpine equilibration in the diamond stability field and evaluation of the $X(CO_2)$ fluid evolu-tion. *Journal of Metamorphic Geology* **25**, 587–603.

Connolly, J. A. D. (1990). Multivariable phase diagrams: an al-gorithm based on generalized thermodynamics. *American Journal of Science* **290**, 666–718.

Connolly, J. A. D. (2009). The geodynamic equation of state: what and how. *Geochemistry, Geophysics, Geosystems* **10**, Q10014.

Connolly, J. A. D. & Trommsdorff, V. (1991). Petrogenetic grids for metacarbonate rocks: pressure–temperature phase-diagrams for mixed-volatile systems. *Contributions to Mineralogy and Petrology* **108**, 93–105.

Connolly, J. A. D., Memmi, I., Trommsdorff, V., Franceschelli, M. & Ricci, C. A. (1994). Forward modeling of calc-silicate microinclusions and fluid evolution in a graphitic metape-lite, northeast Sardinia. *American Mineralogist* **79**, 960–972.

Cossio, R., Borghi, A. & Ruffini, R. (2002). Quantitative modal determination of geological samples based on X-ray multie-lemental map acquisition. *Microscopy and Microanalysis* **8**, 139–149.

Cottle, J. M., Waters, D. J., Riley, D., Beyssac, O. & Jessup, M. J. (2011). Metamorphic history of the South Tibetan Detachment System, Mt. Everest region, revealed by RSCM thermometry and phase equilibria modelling. *Journal of Metamorphic Geology* **29**, 561–582.

Craw, D. & Upton, P. (2014). Graphite reaction weakening of fault rocks, and uplift of the Annapurna Himal, central Nepal. *Geosphere* **10**, 720–731.

Dasgupta, D. (1993). Contrasting mineral parageneses in high-temperature calc-silicate granulites: example from the Eastern Ghats, India. *Journal of Metamorphic Geology* **11**, 193–202.

de Capitani, C. & Brown, T. H. (1987). The computation of chem-ical equilibrium in complex systems containing non-ideal solutions. *Geochimica et Cosmochimica Acta* **51**, 2639–2652.

de Capitani, C. & Petrakakis, K. (2010). The computation of equi-librium assemblage diagrams with Theriak/Domino soft-ware. *American Mineralogist* **95**, 1006–1016.

Diener, J. F. A. & Powell, R. (2012). Revised activity–composition models for clinopyroxene and amphibole. *Journal of Metamorphic Geology* **30**, 131–142.

Diener, J. F. A., Powell, R., White, R. W. & Holland, T. J. B. (2007). A new thermodynamic model for clino- and orthoamphiboles in the system $Na_2O–CaO–FeO–MgO–Al_2O_3–SiO_2–H_2O–O$. *Journal of Metamorphic Geology* **25**, 631–656.

Evans, K. A. (2011). Metamorphic carbon fluxes: how much and how fast?. *Geology* **39**, 95–96.

Evans, M. J., Derry, L. A. & France-Lanord, C. (2008). Degassing of metamorphic carbon dioxide from the Nepal Himalaya. *Geochemistry, Geophysics, Geosystems* **9**, Q04021.

Ferry, J. M. (1976). Metamorphism of calcareous sediments in the Waterville–Vassalboro area, south–central Maine: min-eral reactions and graphical analysis. *American Journal of Science* **276**, 841–882.

Ferry, J. M. (1980). A case study of the amount and distribution of heat and fluid during metamorphism. *Contributions to Mineralogy and Petrology* **71**, 373–385.

Ferry, J. M. (1983a). On the control of temperature, fluid com-position and reaction progress during metamorphism. *American Journal of Science* **283A**, 201–232.

Ferry, J. M. (1983b). Regional metamorphism of the Vassalboro Formation, south–central Maine, USA: a case study of the role of a fluid in metamorphic petrogenesis. *Journal of the Geological Society, London* **140**, 551–576.

Ferry, J. M. (1986). Reaction progress: a monitor of fluid–rock interaction during metamorphic and hydrothermal events. In: Walther, J. V. & Wood, B. J. (eds) *Fluid–Rock Interactions during Metamorphism*. Springer, pp. 60–88.

Ferry, J. M. (1992). Regional metamorphism of the Waits River Formation, eastern Vermont: delineation of a new type of giant metamorphic hydrothermal system. *Journal of Petrology* **33**, 45–94.

Ferry, J. M. (1994). Overview of the petrologic record of fluid flow during regional metamorphism in northern New England. *American Journal of Science* **294**, 905–988.

Ferry, J. M., Winslow, N. W. & Penniston-Dorland, S. C. (2013). Re-evaluation of infiltration-driven regional metamorphism in northern New England: new transport models with solid solution and cross-layer equilibration of fluid composition. *Journal of Petrology* **54**, 2455–2485.

Fitzsimons, I. C. W. & Harley, S. L. (1994). Garnet coronas in scapolite–wollastonite calc-silicates from East Antarctica: the application and limitations of activity corrected grids. *Journal of Metamorphic Geology* **12**, 761–777.

Gaillardet, J. & Galy, A. (2008). Himalaya—carbon sink or source?. *Science* **320**, 1727–1728.

Ganino, C. & Arndt, N. T. (2009). Climate changes caused by degassing of sediments during the emplacement of large igneous provinces. *Geology* **37**, 323–326.

Ganino, C., Arndt, N. T., Chauvel, C. & Tornos, F. (2014). Metamorphic degassing of carbonates in the contact aureole of the Aguablanca Cu–Ni–PGE deposit, Spain. *Contributions to Mineralogy and Petrology* **168**, 1–21.

Girault, F., Perrier, F., Crockett, R., Bhattarai, M., Koirala, B. P., France-Lanord, C., Agrinier, P., Ader, M., Fluteau, F., Gréau, C. & Moreira, M. (2014). The Syabru–Bensi hydrothermal system in central Nepal: 1. Characterization of carbon dioxide and radon fluxes. *Journal of Geophysical Research: Solid Earth* **119**, 4017–4055.

Goscombe, B. & Hand, M. (2000). Contrasting *P–T* paths in the Eastern Himalaya, Nepal: inverted isograds in a paired metamorphic mountain belt. *Journal of Petrology* **41**, 1673–1719.

Goscombe, B., Gray, D. & Hand, M. (2006). Crustal architecture of the Himalayan metamorphic front in eastern Nepal. *Gondwana Research* **10**, 232–255.

Greenwood, H. J. (1975). Buffering of pore fluids by metamorphic reactions. *American Journal of Science* **275**, 573–593.

Groppo, C., Rolfo, F. & Castelli, D. (2007). Pre-Alpine HT mineral relics in impure marbles from the UHP Brossasco–Isasca Unit (Dora–Maira Massif, western Alps). *Periodico di Mineralogia* **76**, 155–168.

Groppo, C., Rolfo, F. & Lombardo, B. (2009). *P–T* evolution across the Main Central Thrust Zone (Eastern Nepal): hidden discontinuities revealed by petrology. *Journal of Petrology* **50**, 1149–1180.

Groppo, C., Rubatto, D., Rolfo, F. & Lombardo, B. (2010). Early Oligocene partial melting in the Main Central Thrust Zone (Arun Valley, eastern Nepal Himalaya). *Lithos* **118**, 287–301.

Groppo, C., Rolfo, F. & Indares, A. (2012). Partial melting in the Higher Himalayan Crystallines of Eastern Nepal: the effect of decompression and implications for the 'Channel Flow' model. *Journal of Petrology* **53**, 1057–1088.

Groppo, C., Rolfo, F. & Mosca, P. (2013a). The cordierite-bearing anatectic rocks of the Higher Himalayan Crystallines (eastern Nepal): low-pressure anatexis, melt-productivity, melt loss and the preservation of cordierite. *Journal of Metamorphic Geology* **31**, 187–204.

Groppo, C., Rolfo, F., Castelli, D. & Connolly, J. A. D. (2013b). Metamorphic CO_2 production from calc-silicate rocks via

garnet-forming reactions in the CFAS–H_2O–CO_2 system. *Contributions to Mineralogy and Petrology* **166**, 1655–1675.

Grove, T. L., Ferry, J. M. & Spear, F. S. (1983). Phase transitions and decomposition relations in calcic plagioclase. *American Mineralogist* **68**, 41–59.

Grove, T. L., Ferry, J. M. & Spear, F. S. (1986). Phase transitions in calcic plagioclase: A correction and further discussion. *American Mineralogist* **71**, 1049–1050.

Harley, S. L. & Buick, I. S. (1992). Wollastonite–scapolite assemblages as indicators of granulite pressure–temperature–fluid history: the Rauer Group, East Antactica. *Journal of Petrology* **33**, 693–728.

Hewitt, D. A. (1973). The metamorphism of micaceous limestones from South–Central Connecticut. *American Journal of Science* **273A**, 444–469.

Holland, T. J. B. & Powell, R. (1998). An internally consistent thermodynamic data set for phases of petrologic interest. *Journal of Metamorphic Geology* **16**, 309–343.

Kellett, D. A., Grujic, D., Warren, C., Cottle, J., Jamieson, R. & Tenzin, T. (2010). Metamorphic history of a syn-convergent orogen-parallel detachment: the south Tibetan detachment system, eastern Himalaya. *Journal of Metamorphic Geology* **28**, 785–808.

Kerrick, D. M. (1974). Review of mixed-volatile (H_2O–CO_2) equilibria. *American Mineralogist* **59**, 729–762.

Kerrick, D. M. & Caldeira, K. (1993). Paleoatmospheric consequences of CO_2 released during early Cenozoic regional metamorphism in the Tethyan orogen. *Chemical Geology* **108**, 201–230.

Kerrick, D. M. & Caldeira, K. (1999). Was the Himalayan orogen a climatically significant coupled source and sink for atmospheric CO_2 during the Cenozoic?. *Earth and Planetary Science Letters* **173**, 195–203.

Kohn, M. J. (2014). Himalayan metamorphism and its tectonic implications. *Annual Review of Earth and Planetary Science* **42**, 381–419.

Kuhn, B. K. (2005). Scapolite stability: Phase relations and chemistry of impure metacarbonate rocks in the Central Alps. PhD thesis, ETH Zürich, 127 pp.

Kuhn, B. K., Reusser, E. & Powell, R. (2005). Metamorphic evolution of calc-schists in the Central Alps, Switzerland. *Schweizerische Mineralogische und Petrographische Mitteilungen* **85**, 175–190.

Leger, A. & Ferry, J. M. (1993). Fluid infiltration and regional metamorphism of the Waits River Formation, northeast Vermont, USA. *Journal of Metamorphic Geology* **11**, 3–29.

Lombardo, B., Pertusati, P. & Borghi, A. (1993). Geology and tectono-magmatic evolution of the eastern Himalaya along the Chomolungma–Makalu transect. In: Treloar, P. J. & Searle, M. P. (eds) *Himalayan Tectonics. Geological Society, London, Special Publications* **74**, 341–355.

López Sánchez Vizcaíno, V., Connolly, J. A. D. & Gómez-Pugnaire, M. T. (1997). Metamorphism and phase relations in carbonate rocks from the Nevado–Filá bride Complex (Cordilleras Béticas, Spain): application of the Ttn + Rt + Cal + Qtz + Gr buffer. *Contributions to Mineralogy and Petrology* **126**, 292–302.

Mathavan, V. & Fernando, G. W. A. R. (2001). Reactions and textures in grossular–wollastonite–scapolite calc-silicate granulites from Maligawila, Sri Lanka: evidence for high temperature isobaric cooling in the meta-sediments of the Highland Complex. *Lithos* **59**, 217–232.

Mörner, N. A. & Etiope, G. (2002). Carbon degassing from the lithosphere. *Global and Planetary Change* **33**, 185–203.

Mosca, P., Groppo, C. & Rolfo, F. (2012). Structural and metamorphic features of the Main Central Thrust Zone and its contiguous domains in the eastern Nepalese Himalaya.

Journal of the Virtual Explorer, Electronic Edition **41**, paper 2.

Mosca, P., Groppo, C. & Rolfo, F. (2014). The geology between Khimti Khola and Likhu Khola valleys: a field trip along the Numbur Cheese Circuit (central–eastern Nepal Himalaya). *Journal of the Virtual Explorer, Electronic Edition* **47**, paper 4.

Nabelek, P. I. (2002). Calc-silicate reactions and bedding-controlled isotopic exchange in the Notch Peak aureole, Utah: implications for differential fluid fluxes with metamorphic grade. *Journal of Metamorphic Geology* **20**, 429–440.

Newton, R. C., Charlu, T. V. & Kleppa, O. J. (1980). Thermochemistry of the high structural state plagioclases. *Geochimica et Cosmochimica Acta* **44**, 933–941.

Omori, S., Liou, J. G., Zhang, R. Y. & Ogasawara, Y. (1998). Petrogenesis of impure dolomitic marble from the Dabie Mountains, central China. *Island Arc* **7**, 98–114.

Perrier, F., Richon, P., Byrdina, S., France-Lanord, C., Rajaure, S., Koirala, B. P., Shrestha, P. L., Gautam, U. P., Tiwari, D. R., Revil, A., Bollinger, L., Contraires, S., Bureau, S. & Sapkota, S. N. (2009). A direct evidence for high carbon dioxide and radon-222 discharge in Central Nepal. *Earth and Planetary Science Letters* **278**, 198–207.

Pognante, U. & Benna, P. (1993). Metamorphic zonation, migmatization, and leucogranites along the Everest transect (eastern Nepal and Tibet): record of an exhumation history. In: Treloar, P. J. & Searle, M. P. (eds) *Himalayan Tectonics. Geological Society, London, Special Publications* **74**, 323–340.

Pouchou, J. L. & Pichoir, F. (1988). Determination of mass absorption coefficients for soft X-rays by use of the electron microprobe. In: *Microbeam Analysis*. San Francisco Press, pp. 319–324.

Powell, R., Holland, T. J. B. & Worley, B. (1998). Calculating phase diagrams involving solid solutions via non-linear equations, with examples using THERMOCALC. *Journal of Metamorphic Geology* **16**, 577–588.

Rice, J. M. & Ferry, J. M. (1982). Buffering, infiltration, and control of intensive variables during metamorphism. In: Ferry, J. M. (ed.) *Characterization of Metamorphism through Mineral Equilibria. Mineralogical Society of America, Reviews in Mineralogy* **10**, 263–326.

Robinson, P. (1991). Eye of the petrographer, mind of the petrologist. *American Mineralogist* **76**, 1781–1810.

Rolfo, F., Groppo, C., Mosca, P., Ferrando, S., Costa, E. & Kaphle, K. P. (2015). Metamorphic CO_2 degassing in the active Himalayan orogen: exploring the influence of orogenic activity on the long-term global climate changes. In: Lollino, G. et al. (eds) *Engineering Geology for Society and Territory, Vol. 1*. Springer, pp. 21–25.

Rolfo, F., Groppo, C. & Mosca, P. (2017). Metamorphic CO_2 production in calc-silicate rocks from the eastern Himalaya. *Italian Journal of Geosciences*, in press, doi:10.3301/IJG.2015.36.

Satish Kumar, M. & Harley, S. L. (1998). Reaction textures in scapolite–wollastonite–grossular calc-silicate rock from the Kerala Khondalite Belt, Southern India: evidence for high-temperature metamorphism and initial cooling. *Lithos* **44**, 83–99.

Schmädicke, E., Okrusch, M., Schubert, W., Elwart, B. & Görke, U. (2001). Phase relations of calc-silicate assemblages in the Auerbach marble, Odenwald Crystalline Complex, Germany. *Mineralogy and Petrology* **72**, 77–111.

Searle, M. P., Law, R. D., Godin, L., Larson, K. P., Streule, M. J., Cottle, J. M. & Jessup, M. J. (2008). Defining the Himalayan Main Central Thrust in Nepal. *Journal of the Geological Society, London* **165**, 523–534.

Sengupta, P. & Raith, M. M. (2002). Garnet stoichiometry as petrogenetic indicator: an example from the marble–calc-silicate interface from Kondapalle, Eastern Ghats Belt. *American Journal of Science* **302**, 686–725.

Sengupta, P., Sanyal, S., Dasgupta, S., Fukuoka, M. & Ehl, J. (1997). Controls of mineral reactions in high-grade garnet–wollastonite–scapolite-bearing calcsilicate rocks: an example from Anakapalle, Eastern Ghats, India. *Journal of Metamorphic Geology* **15**, 551–564.

Shrestha, S. B., Shrestha, J. N. & Sharma, S. R. (1984). *Geological map of Eastern Nepal, 1:250000*. Ministry of Industry, Department of Mines and Geology.

Skelton, A. (2011). Flux rates for water and carbon during greenschist facies metamorphism. *Geology* **39**, 43–46.

Skelton, A. (2013). Is orogenesis a net sink or source of atmospheric CO_2?. *Geology Today* **29**, 102–107.

Skippen, G. B. (1971). Experimental data for reactions in siliceous marbles. *Journal of Geology* **79**, 457–481.

Skippen, G. B. (1974). An experimental model for low pressure metamorphism of siliceous dolomitic marble. *American Journal of Science* **274**, 487–509.

Skippen, G. B. & Hutcheon, I. (1974). The experimental calibration of continuous reactions in siliceous carbonate rocks. *Canadian Mineralogist* **12**, 327–333.

Spear, F. S., Kohn, M. J. & Cheney, J. T. (1999). *P–T* paths from anatectic pelites. *Contributions to Mineralogy and Petrology* **134**, 17–32.

Stephenson, N. C. N. & Cook, N. D. J. (1997). Metamorphic evolution of calcsilicate granulites near Battye Glacier, northern Prince Charles Mountains, East Antarctica. *Journal of Metamorphic Geology* **15**, 361–378.

Svensen, H. & Jamtveit, B. (2010). Metamorphic fluids and global environmental changes. *Elements* **6**, 179–182.

Tajcmanova, L., Connolly, J. A. D. & Cesare, B. (2009). A thermodynamic model for titanium and ferric iron solution in biotite. *Journal of Metamorphic Geology* **27**, 153–165.

Trommsdorff, V. (1972). Change in *T–X* during metamorphism of siliceous rocks of the Central Alps. *Schweizerische Mineralogische und Petrographische Mitteilungen* **52**, 567–571.

Visonà, D. & Lombardo, B. (2002). Two mica- and tourmaline leucogranites from the Everest–Makalu region (Nepal–Tibet): Himalayan leucogranite genesis by isobaric heating?. *Lithos* **62**, 125–150.

Winter, J. D. (2010). *Principles of Igneous and Metamorphic Petrology*, 2nd edn. Prentice Hall.

Whitney, D. L. & Evans, B. W. (2010). Abbreviations for names of rock-forming minerals. *American Mineralogist* **95**, 185–187.

AQ6

AQ7

AQ8